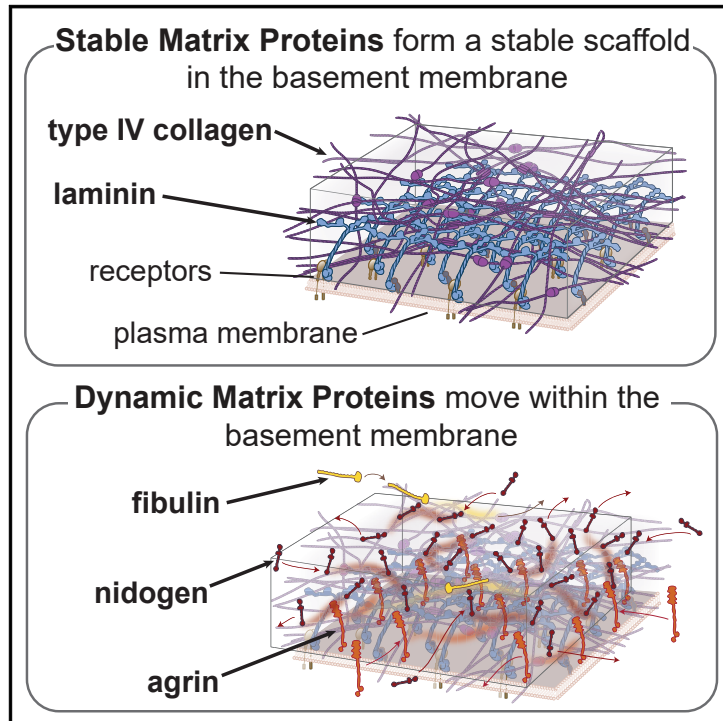


# Developmental Cell

## Comprehensive Endogenous Tagging of Basement Membrane Components Reveals Dynamic Movement within the Matrix Scaffolding

### Graphical Abstract



### Authors

Daniel P. Keeley, Eric Hastie, Ranjay Jayadev, ..., Jonathan L. Jeger, Brenton D. Hoffman, David R. Sherwood

### Correspondence

david.sherwood@duke.edu

### In Brief

Basement membranes (BMs) are complex extracellular structures that are difficult to study *in vivo*. Keeley et al. use CRISPR-Cas9 genome editing to fluorescently tag 29 BM components in *C. elegans* and discover that BMs are not static—many matrix proteins move within a stable laminin and collagen IV-based scaffold.

### Highlights

- *In vivo* visualization of 29 basement membrane (BM) proteins fused with mNeonGreen
- Embryonic BMs share a common template but diversify greatly during development
- Stable BM proteins form a scaffold that supports movement of dynamic BM components
- Papilin promotes local BM collagen removal by limiting GON-1 protease localization

Article

# Comprehensive Endogenous Tagging of Basement Membrane Components Reveals Dynamic Movement within the Matrix Scaffolding

Daniel P. Keeley,<sup>1,5</sup> Eric Hastie,<sup>1,5</sup> Ranjay Jayadev,<sup>1,5</sup> Laura C. Kelley,<sup>1</sup> Qiuyi Chi,<sup>1</sup> Sara G. Payne,<sup>1,2</sup> Jonathan L. Jeger,<sup>1</sup> Brenton D. Hoffman,<sup>3</sup> and David R. Sherwood<sup>1,4,6,\*</sup>

<sup>1</sup>Department of Biology, Duke University, Box 90338, Durham, NC 27708, USA

<sup>2</sup>Department of Cell Biology, Duke University, Box 3709, Durham, NC 27710, USA

<sup>3</sup>Department of Biomedical Engineering, Duke University, Box 90281, Durham, NC 27708, USA

<sup>4</sup>Regeneration Next Initiative, Duke University, Durham, NC 27710, USA

<sup>5</sup>These authors contributed equally

<sup>6</sup>Lead Contact

\*Correspondence: [david.sherwood@duke.edu](mailto:david.sherwood@duke.edu)

<https://doi.org/10.1016/j.devcel.2020.05.022>

## SUMMARY

Basement membranes (BMs) are supramolecular matrices built on laminin and type IV collagen networks that provide structural and signaling support to tissues. BM complexity, however, has hindered an understanding of its formation, dynamics, and regulation. Using genome editing, we tagged 29 BM matrix components and receptors in *C. elegans* with mNeonGreen. Here, we report a common template that initiates BM formation, which rapidly diversifies during tissue differentiation. Through photobleaching studies, we show that BMs are not static—surprisingly, many matrix proteins move within the laminin and collagen scaffoldings. Finally, quantitative imaging, conditional knockdown, and optical highlighting indicate that papilin, a poorly studied glycoprotein, is the most abundant component in the gonadal BM, where it facilitates type IV collagen removal during BM expansion and tissue growth. Together, this work introduces methods for holistic investigation of BM regulation and reveals that BMs are highly dynamic and capable of rapid change to support tissues.

## INTRODUCTION

Basement membranes (BMs) are thin, dense sheets of extracellular matrix (ECM) that surround most tissues (Yurchenco, 2011). Comparative phylogenetic studies have suggested that BMs are the most ancient ECM and arose at the time of animal multicellularity (Fidler et al., 2018). BMs are supramolecular assemblies composed of a core set of proteins that includes laminin networks, cross-linked type IV collagen grids, the glycoprotein nidogen, and often the heparan sulfate proteoglycans perlecan, agrin, and type XVIII collagen. Matricellular proteins, such as fibulins and secreted protein acidic and rich in cysteine (SPARC), proteases, protease inhibitors, and growth factors, are also BM residents (Yurchenco, 2011). Numerous receptors, including integrin and dystroglycan, interact with BM matrix components to mediate laminin polymerization in embryonic cells, an event necessary to seed initial BM formation (Yurchenco, 2015). BMs have numerous essential structural roles in animals—they bear load to protect tissues from mechanical forces, filter blood in the kidney, help form the blood-brain barrier and neuromuscular junctions, and mediate tissue shaping (Morrissey and Sherwood, 2015; Rogers and Nishimune, 2017). BMs also have crucial

signaling activities that polarize epithelia, regulate tissue growth, guide cell migration, and promote cell survival (Bunt et al., 2010; Li et al., 2017; Ma et al., 2017; Rasmussen et al., 2012). To achieve distinct functions, BMs vary significantly in composition, thickness, and mechanical properties (Chang and Chaudhuri, 2019). More than 20 distinct human diseases are associated with genetic disruption of BM components, highlighting the diverse and important roles of BMs (Nyström et al., 2017). The misregulation of BM component expression is also a key driver of cancer metastasis, and defective BM turnover leads to tissue decline in diabetes mellitus, fibrosis, and aging (Candiello et al., 2010; Halfter et al., 2017; Naba et al., 2014).

Despite the fundamental importance of BMs to development, homeostasis, and disease, mechanisms regulating their structure, growth, and turnover are poorly understood. BMs interact dynamically with tissues and thus require *in vivo* models to elucidate their regulation and function. Further, as each BM is a unique assemblage of matrix components, experimental approaches that address the complete makeup of BMs *in vivo* are needed. Because of BM compositional complexity, most studies have focused on only a handful of components. Mass spectrometry approaches combined with bioinformatics are

beginning to characterize the complete ECM-associated with tissues (Schiller et al., 2015), but limitations include challenges with protein contamination, solubility, identification, and confirmation of matrix proteins as bona fide BM inhabitants (Randles et al., 2017).

There is also a gap in our understanding of BM component dynamics. Previous work on BM turnover using pulse-chase experiments suggests that BMs turn over on a scale of weeks (Decaris et al., 2014; Trier et al., 1990). Although these studies indicate that BM matrix components are stable and have long half-lives, they have not revealed whether matrix components are fixed in place once deposited within BMs. Live cell imaging in *Drosophila* with GFP-tagged type IV collagen, perlecan, nidogen, and laminin has revealed dynamic mechanisms of matrix deposition during egg chamber formation and initial BM assembly (Isabella and Horne-Badovinac, 2016; Matsubayashi et al., 2017). However, endogenously tagged BM matrix proteins are limited in *Drosophila* to only type IV collagen and perlecan (Ramos-Lewis et al., 2018) and BM-encased organs in larvae and adults lie deep within tissues beyond the reach of light microscopy, hindering analysis of matrix dynamics after deposition (Cetera et al., 2016).

*Caenorhabditis elegans* is a powerful model in which to examine BM biology. CRISPR-Cas9-mediated homologous recombination has facilitated the generation of endogenously tagged laminin, type IV collagen, nidogen, integrin, and dystroglycan genes with genetically encoded fluorophores (Jayadev et al., 2019; Matsuo et al., 2019; Naegeli et al., 2017; Walser et al., 2017). *C. elegans* is also small and translucent, which allows live imaging of BMs from the embryo through adulthood. In addition, unlike vertebrates where BM gene families have expanded, *C. elegans* has single genes encoding most major BM components, simplifying genetic and compositional studies (Clay and Sherwood, 2015). Finally, RNAi-mediated knockdown allows for conditional loss of BM components, facilitating later functional studies of BM components required for embryonic viability (Morrisey et al., 2016).

To comprehensively examine BMs, we used genome engineering to introduce mNeonGreen (mNG) into the genomic loci encoding 17 BM matrix components and 12 receptors. We show that a similar template of matrix components and receptors is associated with initial BM formation throughout the embryo shortly after gastrulation, but then BMs diversify dramatically on tissues as development proceeds. By performing fluorescent recovery after photobleaching (FRAP), we demonstrate that BMs consist of a stable scaffolding of collagen and laminin, within which the matrix proteins nidogen, fibulin, agrin, spondin, and peroxidasin move, thus revealing an unexpected dynamic property of BMs. Finally, we address a poorly understood aspect of BM biology—BM expansion during organ growth. Using quantitative live imaging and conditional knockdown, we reveal that the glycoprotein papilin is the most abundant matrix component within the rapidly growing gonadal BM, and that loss of papilin results in smaller gonads and type IV collagen accumulation into a fibrotic network during BM growth. Through optical highlighting of type IV collagen, we show that papilin promotes collagen removal during BM expansion, and that papilin functions in part by limiting BM access of collagen-modifying ADAMTS (a disintegrin and metalloproteinase with

thrombospondin motifs) proteins. Together, this collection of endogenously tagged BM components provides a new resource to investigate BM formation, diversity, and regulation and reveals that BMs are not static after deposition but rather have highly mobile components that may confer dynamic properties to BMs.

## RESULTS

### Endogenous, Fluorescently Tagged BM Proteins

The properties and regulation of BMs remain elusive in part because of the challenge of studying BM composition and dynamics *in vivo*. *C. elegans* is a useful model to examine BMs due to its optical clarity, amenability to genome editing, and conserved BM gene families that have not undergone the expansion found in vertebrates (Clay and Sherwood, 2015). To better understand BM regulation, we used CRISPR-Cas9-mediated homologous recombination to knock in genetically encoded fluorescent proteins into 29 genes encoding conserved matrix components and receptors in *C. elegans* (Figures 1, S1, and S2; Table S1) (Dickinson and Goldstein, 2016; Gotenstein et al., 2010; Hrus et al., 2007; Kramer, 2005; Topf and Chiquet-Ehrismann, 2011; Unsoeld et al., 2013). These genes encode: (1) the core BM components laminin ( $\alpha$ A/C. *elegans* LAM-3,  $\alpha$ B/EPI-1,  $\beta$ /LAM-1,  $\gamma$ /LAM-2), type IV collagen ( $\alpha$ 1/EMB-9 and  $\alpha$ 2/LET-2), perlecan/UNC-52, agrin/AGR-1, nidogen/NID-1, collagen XVIII/CLE-1); (2) the matricellular proteins SPARC/OST-1, fibulin/FBL-1, spondin/SPON-1, papilin/MIG-6, hemicentin/HIM-4; (3) the peroxidasin enzymes (*C. elegans* PXN-1 and PXN-2, herein referred to as peroxidasin-1 and peroxidasin-2); and (4) BM-associated receptors, including integrins ( $\alpha$ /INA-1,  $\alpha$ /PAT-2, and  $\beta$ /PAT-3), teneurin/TEN-1, dystroglycan (DGN-1 and DGN-2), syndecan/SDN-1, glypicans (GPN-1 and LON-2), LAR phosphatase/PTP-3, and discoidin domain receptors (DDR-1 and DDR-2) (Figure 1; Table S1). All genes were tagged with mNG to allow for direct comparisons of protein levels by fluorescence intensity. Select genes were tagged with the red fluorophore mKate2 (Figures S1 and S2; Table S1) (Heppert et al., 2016). Most fluorophores were attached at the C terminus with an 18-amino acid non-polar flexible linker, although some were inserted N-terminally or internally to visualize multiple splice variants or avoid post-translational cleavage (Figures S1 and S2; Table S1; see below).

To determine the validity of our tagging approach, we assessed knockin strain viability and tagged BM protein localization (Table S1). For the majority of genes, insertion of the fluorophore resulted in superficially wild-type homozygous viable animals. However,  $\alpha$ 2-type IV collagen/*let-2*::mNG and SPARC/*ost-1*::mNG animals were non-viable as homozygotes and  $\beta$ -laminin/*lam-1*::mNG worms grew slowly. These strains were thus maintained as heterozygotes. The vast majority of proteins localized to BM. However, in four cases (papilin/*mig-6* N-terminal, perlecan/*unc-52* C- and N-terminal, and peroxidasin-2/*pxn-2* C-terminal), the mNG signal localized diffusely in the extracellular space and was cleaved from the protein (Figures S1 and S3). Alternative tagging of papilin C-terminal, peroxidasin-2/*pxn-2* N-terminal, and perlecan internal localized tightly to BM (Table S1; Figure S1). Further, western blotting confirmed

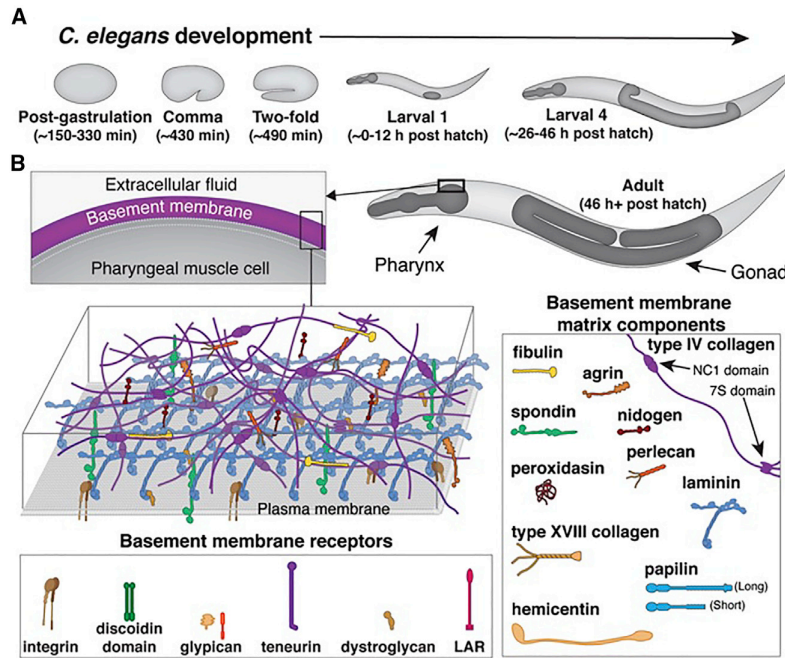


**Figure 1. BM Matrix Components and Receptors in *C. elegans***

(A) A schematic of the embryonic and larval stages of the *C. elegans* life cycle labeled with developmental times post-fertilization (embryonic stages) or post-hatching (larval stages) at 20°C with the pharynx and gonad highlighted.

(B) A schematic of BM composition showing the major families of conserved BM matrix components and receptors in *C. elegans* that were endogenously tagged using genome editing. See [STAR Methods](#) for details on molecule illustrations.

full-length papilinL/MIG-6L::mNG protein (Figure S3). We used these tagged strains for subsequent studies. These results demonstrate that endogenously tagging BM components with genetically encoded fluorophores is a viable approach for study of BMs *in vivo*.

### BM Emergence during Development

Studies in mice, *C. elegans*, and *Drosophila* embryos have indicated that laminin network formation is a requirement for initiation of BM formation (Huang et al., 2003; Matsubayashi et al., 2017; Smyth et al., 1999; Urbano et al., 2009). Cell culture work has also suggested that integrin and dystroglycan receptors mediate laminin polymerization (Yurchenco and Patton, 2009). *In vivo* studies have shown that the embryonic type IV collagen network is deposited after laminin in mice, *C. elegans*, and *Drosophila* (Graham et al., 1997; Matsubayashi et al., 2017; Pöschl et al., 2004; Urbano et al., 2009). The timing of the appearance of other BM components and matricellular proteins within embryonic BMs is less clear.

To better understand how BMs are assembled during embryogenesis, we used our collection of endogenously tagged BM components to view BM emergence. *C. elegans* embryonic development takes 14 h from fertilization to hatching at 20°C (Figure 1A) (Hall et al., 2017). The primordial intestine, muscle, epidermis, and pharynx (contractile feeding organ) begin to assemble during gastrulation (150–330 min) (Figure 2) (Hall et al., 2017). Following gastrulation, the embryo elongates, progressing through comma (430 min) and 2-fold stages (490 min; Figure 2) during which the nerve ring encircles the pharynx prior to hatching (840 min).  $\gamma$ -laminin, nidogen, and papilin were the first detectable BM components and were deposited around all tissues by the end of gastrulation (Figures 2 and S4). *C. elegans* has two  $\alpha$ -laminins (LAM-3 and EPI-1) that pair

with the shared  $\beta$  (LAM-1) and  $\gamma$  (LAM-2) chains (Huang et al., 2003; Kao et al., 2006). Both  $\alpha$ -laminin chains were present in the primordial gut and pharynx, but only the  $\alpha$ -laminin EPI-1 was in the muscle and epidermal BM. Additionally, the two isoforms of papilin were distributed differently—papilinL was in all BMs, whereas papilinS was restricted to the BM surrounding the body wall muscle (Figures 2 and S4). The integrins and dystroglycan were broadly distributed on all tissues at gastrulation. *C. elegans* has a single dystroglycan receptor, DGN-1 and two integrin heterodimers composed of either the  $\alpha$ -integrins INA-1 or PAT-2 with the single  $\beta$ -integrin PAT-3 (Clay and Sherwood, 2015). The  $\alpha$ -integrin PAT-2 localized strongly to muscle, whereas INA-1 was found along gut and pharynx surfaces. The  $\beta$ -integrin PAT-3 localized to all three tissues (Figures 2 and S5). Other BM-associated receptors present early appeared to be localized intracellularly (DDR-1 and DDR-2) or to cell-cell membrane interfaces (syndecan/SDN-1 and LAR phosphatase/PTP-3), where they might mediate intercellular communication (Figures 2 and S4). Together, these observations indicate that at BM emergence, a common extracellular laminin, nidogen, and papilin scaffold forms on all tissues while integrin and dystroglycan receptors localize to all BM-associated cell surfaces. Notably, even at initial BM formation, heterogeneities in laminin, papilin, and integrin isoforms distinguish nascent BMs.

As embryonic development proceeded to the comma stage, type IV collagen appeared in all three BMs (it was also present at this stage and later stages in large intracellular vesicles within body wall muscles, see Morrissey et al., 2016), perlecan localized to the body wall muscle BM, and agrin became visible in the pharynx BM (Figures 2 and S4). Dystroglycan and the integrin receptors maintained their localization, while DDR-1 localized to BMs in the muscle and intestine and the glypican LON-2 was present along the pharynx BM (Figures 2 and S5). By the 2-fold stage, the nerve ring develops and many BM-associated receptors are enriched there, including the integrins, LAR phosphatase, glypican, and syndecan (Figures 2 and S5). The nerve ring BM also had high levels of all laminin chains, agrin, nidogen, type IV collagen, SPARC, papilin, and type XVIII collagen (Figures 2 and S5). Finally, the peroxidasins, hemicentin, and fibulin were only detected within BMs after embryonic



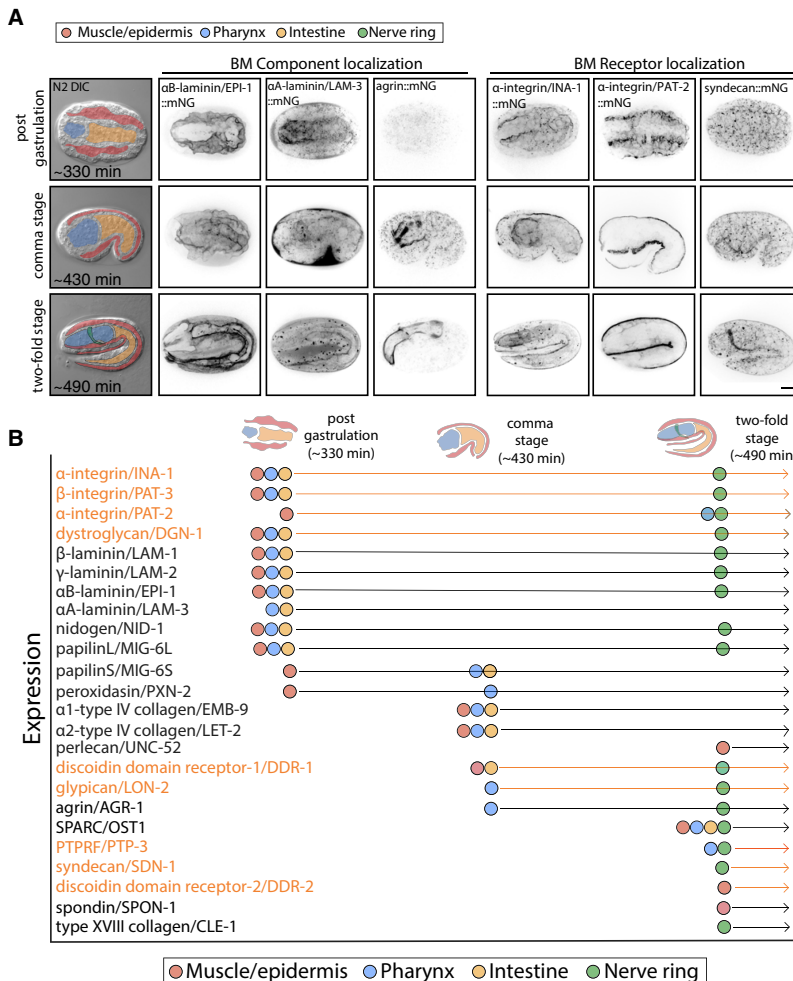


**Figure 2. BM Emergence during Development**

(A) The left column shows differential interference contrast (DIC) images of embryonic development at 20°C at the post-gastrulation (330 min post-fertilization), comma (430 min), and 2-fold stages (490 min). Color overlays highlight embryonic muscle and epidermis (red), pharynx (blue), intestine (yellow), and the nerve ring when it arises at the 2-fold stage (green). The muscle and epidermis are colored together as they were difficult to differentiate; however, clear associations with muscle are noted in the text. Inverted gray-scale maximum intensity projections show fluorescence localization of representative BM components (columns 2–4)—the  $\alpha$ -laminin subunits (EPI-1 and LAM-3) and agrin/AGR-1. EPI-1 localizes to the BM of all tissues starting from the end of gastrulation, while LAM-3 shows a similar pattern but is absent from muscle/epidermis and the nerve ring. Agrin is restricted to the pharynx BM starting at the comma stage. Maximum intensity projections (with single z slice shown for PAT-2 at 2-fold stage) of BM receptor localization (columns 5–7) of the  $\alpha$ -integrins (INA-1 and PAT-2) and syndecan/SDN-1. INA-1 localizes to cell-BM interface of all tissues, while PAT-2 appears at the muscle-BM interface at gastrulation then later at the pharynx and nerve ring BM. Scale bar represents 10  $\mu$ m.

(B) A graphic summary of matrix component (black) and matrix receptor (orange) localization during embryonic development ( $n > 5$  animals examined for each stage and each BM component). Arrows represent developmental progress and dots represent the stage of emergence in each tissue.

is a nascent organ that envelops the germ cell and somatic gonad precursors. It grows rapidly during larval development and is encased by a thinner BM (Huang et al., 2003). Measurements along the pos-

terior bulb of the pharynx and central dorsal region of the gonad showed that the core BM components laminin ( $\gamma$ -laminin::mNG), type IV collagen ( $\alpha$ 1-type IV collagen::mNG), and nidogen were present in both organs, as well as papilinS and type XVIII collagen (Figure 3B). The  $\alpha$ 1 chain of type IV collagen (EMB-9) is present in two copies per type IV collagen molecule, while the  $\gamma$ -chain of laminin (LAM-2) is one of three chains of laminin (Kramer, 2005). For simplicity, unless denoted, we refer to levels and presence of EMB-9/ $\alpha$ 1-type IV collagen::mNG as type IV collagen and LAM-2/ $\gamma$ -laminin::mNG as laminin in the text. PapilinS was the most abundant component in both BMs. Spondin, fibulin, agrin, perlecan, and peroxidasin-1 were present in the pharynx BM, but not the gonad (Figure 3B). Direct comparisons of BM component levels revealed that every matrix protein that was present in both tissues was higher in the pharynx, except for papilinS (Figure 3B). The most dramatic difference was in type IV collagen levels, which were ~3-fold higher in the pharynx BM (Jayadev et al., 2019). Given the size of type IV collagen (~400 nm) (Yurchenco, 2011), it may account for the greater thickness of the pharynx BM. Most matrix components in the pharynx BM were also present in gradients or enriched in

### Quantitative Analysis and Comparisons of BM Composition between Tissues

BM composition increases significantly over developmental time as tissues differentiate. BMs are diverse in composition and changes in BMs influence cell and tissue function in normal and disease states (Naba et al., 2014; Randles et al., 2017). Biochemical, mass spectrometry, and fixed tissue microscopy studies have characterized important aspects of BM structure and composition; however, these approaches cannot easily determine the relative amounts of multiple BM components at defined locations and none can be used in living animals.

We next used our endogenously tagged BM matrix components to quantify and compare BM composition surrounding two different organs: the L1 larval stage pharynx and gonad (Figure 3). The pharynx is a rigid muscular pump that continuously beats to grind food. It is fully functional at the L1 stage, and electron microscopy studies have indicated the pharynx has a thick BM (Huang et al., 2003; Mango, 2007). In contrast, the L1 gonad

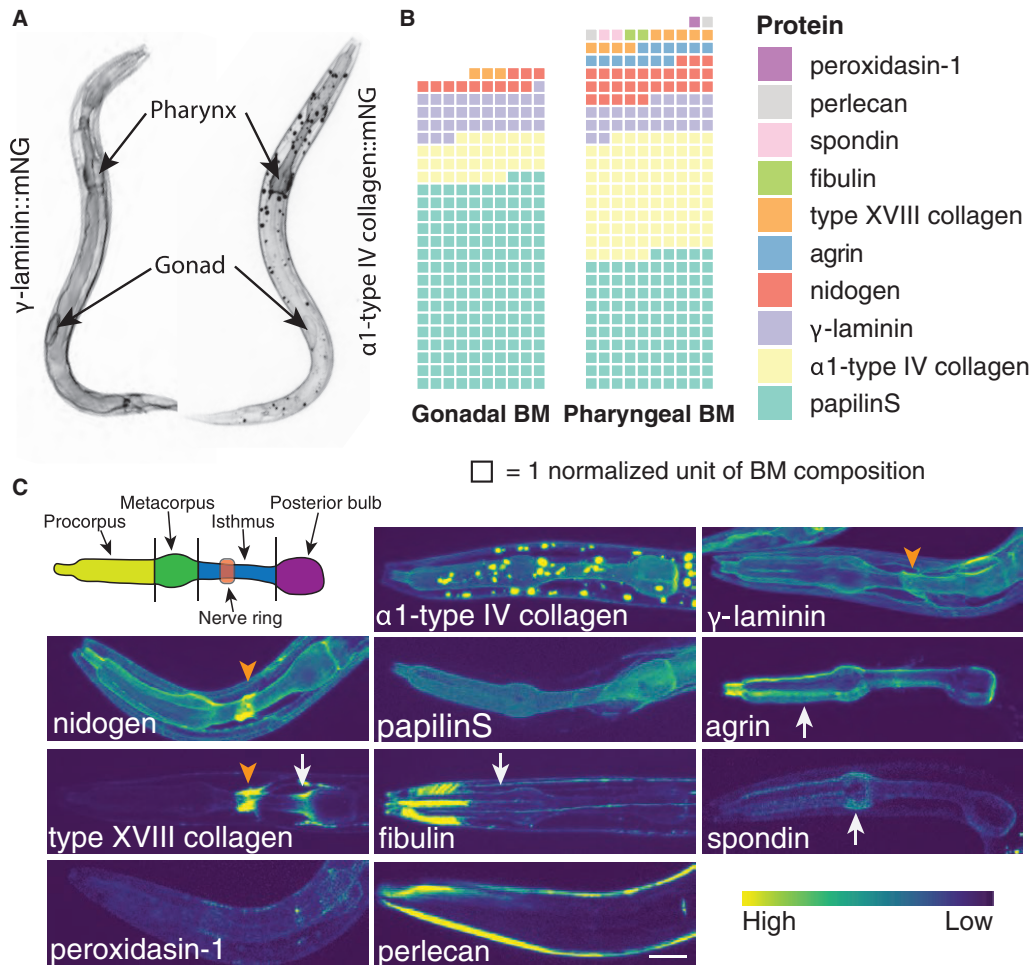


**Figure 3. Quantification of BM Composition and Regional Localization**

(A) Representative inverted gray-scale maximum intensity confocal projections of whole animal  $\gamma$ -laminin::mNG (left) and  $\alpha$ 1-type IV collagen::mNG (right) at the L1 stage.

(B) Normalized mean fluorescence intensity displayed as waffle plots compare the composition of the gonadal and pharynx BMs per unit area. Each square is normalized to the mean fluorescence intensity of the least abundant component, peroxidasin-1 ( $n > 9$  animals imaged for each matrix component).

(C) Heatmaps of maximum intensity projections from confocal z stacks of the L1 pharynx enlarged to emphasize regional differences (see schematic) in protein distribution—type IV collagen is in a gradient from posterior to anterior, laminin and nidogen are evenly distributed (but concentrated around nerve ring, orange arrowheads), papilinS is evenly distributed (signal from the epidermis makes it appear higher in the posterior bulb), agrin is enriched in the anterior region (arrow), type XVIII collagen is at high levels in the posterior bulb (white arrow, and also in nerve ring BM, orange arrowhead), fibulin is enriched in the anterior region (arrow), spondin is enriched in the metacarpus (arrow), and peroxidasin-1 and perlecan are present at low uniform levels ( $n = 10$  animals examined for each). Scale bar represents 10  $\mu$ m.

specific sub-regions, indicating specialization within the pharynx BM (Figure 3C). Collectively, these results show that BMs vary in quantitative composition; that the makeup of the pharynx BM, which surrounds a functional tissue, is more complex than that of the immature gonad, and that BM composition can change across micron-scale distances.

#### A Stable Collagen and Laminin Scaffold Supports Mobile BM Proteins

Previous work in vertebrates suggests that BMs turn over on a scale of weeks (Decaris et al., 2014; Trier et al., 1990). Whether matrix components are stably integrated within BMs or have dy-

namic associations after BMs are deposited, however, is unknown. To directly address the stability of individual BM matrix components, we performed FRAP experiments in the posterior bulb of the pharynx BM of L4-staged larvae (Figure 4A). We chose the pharynx as it contains most BM matrix components we tagged (perlecan levels, however, were too low to assess), it does not grow significantly during the L4 larval stage, and the different matrix component levels do not increase at this time. We hypothesized that fluorescence recovery would measure protein degradation and replacement rates if BM components are stably associated within BM or reveal more rapid dynamic exchange rates if their associations are transient.

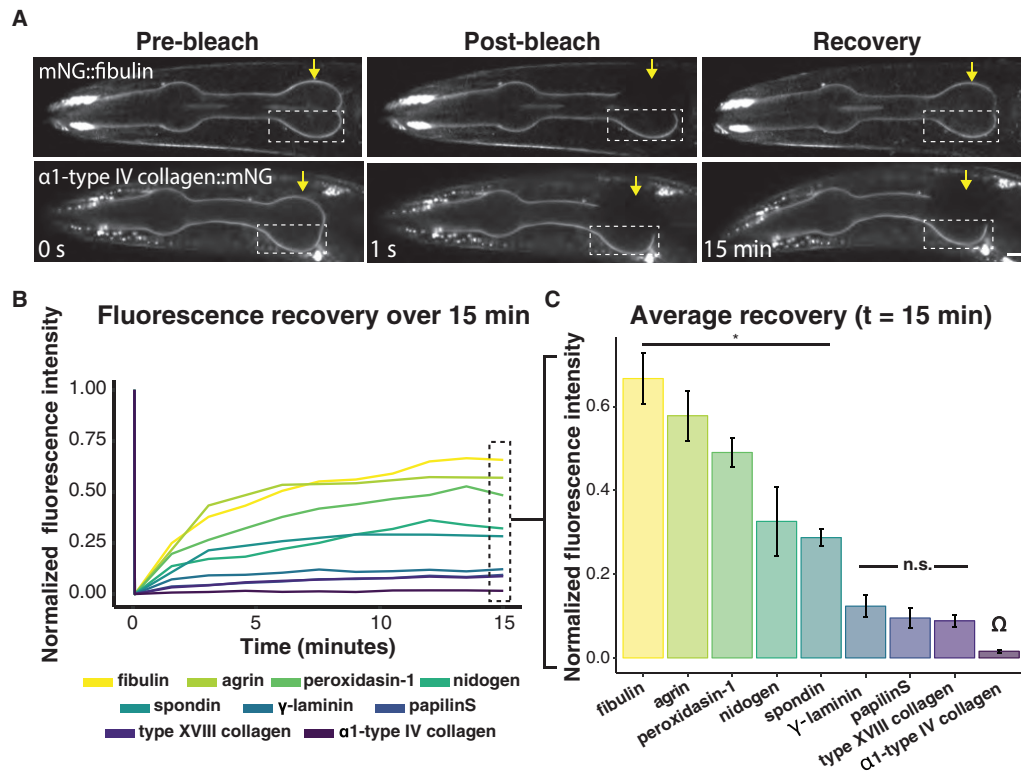


**Figure 4. FRAP of BM Components Reveal Stable and Dynamic Matrix Components**

(A) Confocal images (single z slices) of the L4 pharynx show differences in recovery rate after photobleaching for mNG::fibulin and α1-type IV collagen:mNG over 15 min. Yellow arrows indicate the bleached half of the pharynx and dashed white line indicates the unbleached control region. Scale bar represents 10 μm. (B) Line graph showing the normalized fluorescence recovery of nine BM components present in the L4 pharynx over 15 min (n = 5 animals for each). (C) Bar graph displays the mean recovery fraction for each protein at the end of 15 min. Error bars denote standard error. All means were compared with the α1-type IV collagen as denoted by the Ω symbol. Black bars indicate two groups: × mNG::fibulin, agrin-1::mNG, peroxidasin-1::mNG, nidogen::mNG, and spondin::mNG exhibited faster recovery than α1-type IV collagen (n = 5 animals for each, \*p < 0.005, Dunnett's test); however, no significant (n.s.) differences were observed for γ-laminin::mNG, papilinS::mNG, and α1-type XVIII collagen::mNG.

To determine if any matrix components show transient connections, we analyzed fluorescence recovery over a 15-min period, imaging every 90 s. Fibulin, agrin, spondin, nidogen, and peroxidasin-1 recovered ~30%–65% of their original fluorescence intensity in only 15 min. In contrast, laminin, type XVIII collagen, papilinS, and type IV collagen exhibited ~10% or less recovery over this time period (Figures 4 and S6). Longer imaging revealed that type XVIII collagen and papilinS recovered <20% of their original intensity in 1 h, and laminin and type IV collagen recovered ~30% of their original intensity in 5.5 h, confirming a more stable association with BM (Figure S6). These results indicate that laminin, collagen, and papilinS have a relatively stable association with BM after deposition, whereas all other components have dynamic associations.

We postulated that the rapid recovery seen in many of the BM components was not through protein degradation and replacement, as BM proteins have long half-lives (Decaris et al., 2014). Consistent with this, western blot analysis confirmed that fibulin, nidogen, agrin, and spondin were present predominantly as full-length mNG fusion proteins (Figure S3). Most matrix proteins in the pharynx BM (with the exception of agrin) are secreted from

distant tissues and recruited to the pharynx BM (Clay and Sherwood, 2015; Gotenstein et al., 2010; Kramer, 2005). We hypothesized that the dynamic BM proteins might be replaced by rapidly exchanging with components in the extracellular fluid, might move within the BM itself, or a combination of both. To test these possibilities, we photobleached the entire posterior bulb of the pharynx and then examined fluorescence recovery every 10 s to assess the initiation of fluorescence recovery (Figure 5). If a matrix protein was predominantly rapidly exchanging with the extracellular fluid, we predicted that it would recover evenly across the bleached region. Alternatively, if the matrix protein moved within the BM, we predicted it would recover first at the edge of the bleached region. Strikingly, all dynamic components—fibulin, nidogen, agrin, spondin, and peroxidasin-1—recovered more quickly near the edge of the bleached region (Figures 5A, S7A, and S7B; Video S1) and moved 5 μm into the unbleached region at rates that closely matched the level of their fluorescence recovery in 15 min: fibulin ( $0.17 \pm 0.04$  μm/s), peroxidasin-1 ( $0.19 \pm 0.02$  μm/s), agrin ( $0.08 \pm 0.02$  μm/s), nidogen ( $0.06 \pm 0.02$  μm/s), and spondin ( $0.09 \pm 0.01$  μm/s; n = 5, mean ± SD). We also examined movement of the bleached fibulin and

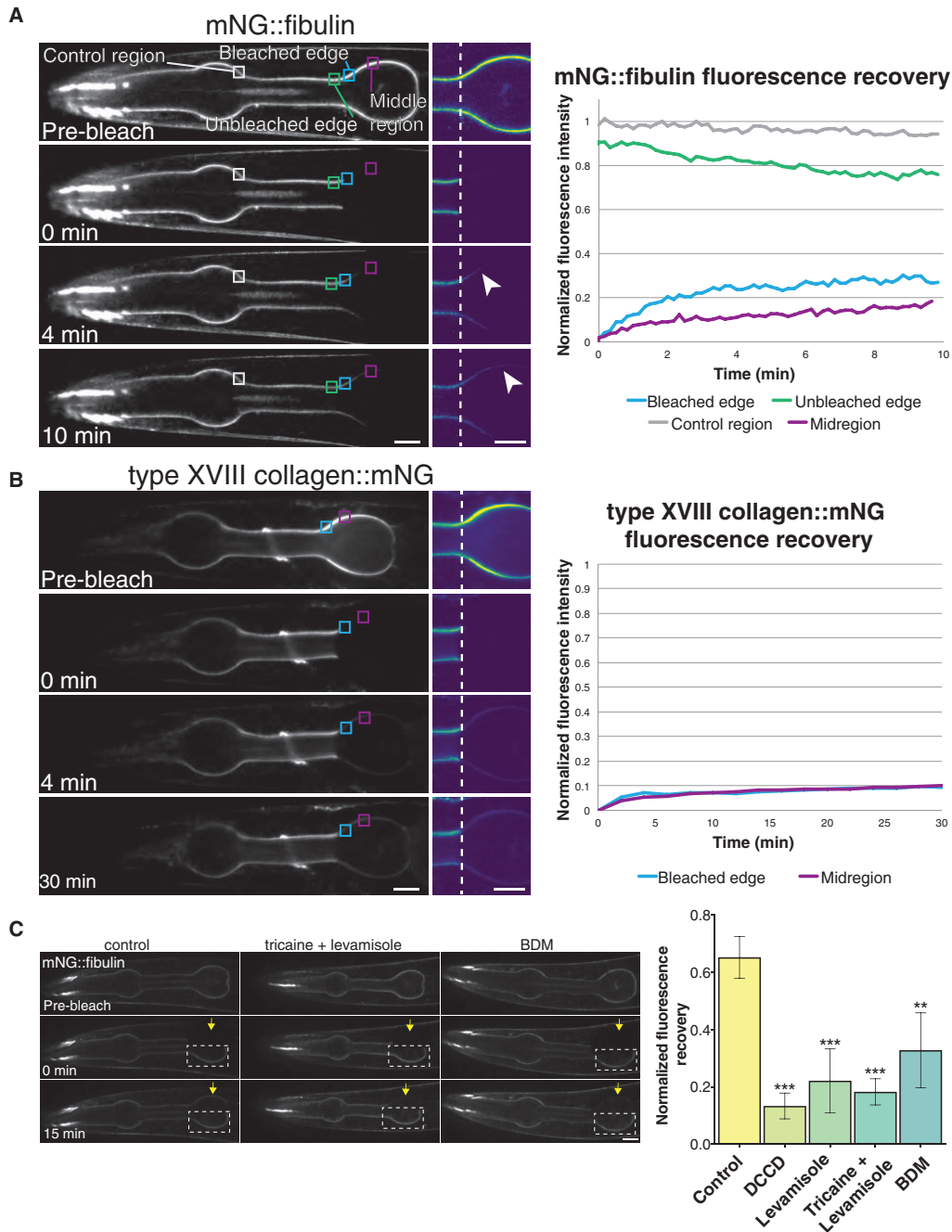


**Figure 5. The Matrix Component Fibulin Moves within the BM**

(A) (Left) A 10-min time lapse (imaged every 10 s) of mNG::fibulin FRAP. Images show a single confocal z slice of the pharynx and an inset of the photobleached region with a heatmap prior to photobleaching (prebleach), after photobleaching (0 min), and at 4- and 10-min recovery time points. Gray boxes represent the control region distant from the bleached area, green boxes the unbleached region of the BM outside the edge of the bleached area, blue boxes the edge of the bleached area, and purple boxes the midregion of the photobleached area. (Right) A line graph of normalized fluorescence recovery reveals that recovery first occurs at the edge of the bleached region (blue) before recovering in the middle (magenta). The graph also shows greater loss of fluorescence in the BM closer to the photobleached region (green) than the control region (gray) ( $n = 5/5$  animals).

(B) (Left) A representative 30-min time lapse (imaged every 2 min) of type XVIII collagen::mNG FRAP and (right) a line graph of recovery. Dim fluorescence signal recovers uniformly across the bleached region independent of proximity to the edge of the bleached region ( $n = 5/5$  animals examined).

(legend continued on next page)



observed that the unbleached fibulin adjacent to the site of photobleaching declined in fluorescence intensity prior to interior regions (presumably as the bleached fibulin moved into this region, [Figure 5A](#)), as would be expected if fibulin moved bi-directionally within the BM. Bleaching the anterior pharynx of *agrin::mNG* worms revealed that *agrin* also moved here ( $n = 5/5$  animals, [Video S2](#)). To further test if matrix movement is a general BM property, we examined the gonadal BM, which contains nidogen (but not other dynamic components; [Figure 3B](#)). Similar to the pharynx BM, nidogen was mobile, whereas laminin did not move ([Figure S7C](#); [Video S3](#)). As a different test to estimate the contribution of matrix components within the extracellular fluid to the recovery of dynamic BM components after photobleaching, we photobleached *mNG::fibulin* in the entire pharynx BM. We examined fibulin as it does not localize strongly to the adjoining gut BM. Thus, the fluorescence recovery should be predominantly from extracellular sources rather than movement within the BM. We found that only  $9.5\% \pm 3.5\%$  of *mNG::fibulin* recovered when the entire pharynx was photobleached compared with  $68.7\% \pm 8.2\%$  recovery when only the posterior bulb was photobleached (mean  $\pm$  SD, 15-min recovery,  $n = 5$ ), suggesting that exchange with the extracellular fluid occurs but is a minor component of dynamic fibulin. Lastly, we determined whether the dynamic recovery of BM components was active or passive, focusing on fibulin, the most dynamic pharynx BM component. We first treated worms with dicyclohexylcarbodiimide (DCCD), an ATP synthase inhibitor, and found that although it did not affect the levels of BM fibulin ([STAR Methods](#)), there was a dramatic reduction in recovery rate after photobleaching ([Figure 5C](#)). We hypothesized that a possible ATP driven regulator of BM movement might be muscle contractions, as these could distribute energy into BMs that surround tissues. Notably, in our FRAP experiments above we immobilized worms with polystyrene beads, which hinders worm movement but allows for muscle contractions. Strikingly, we found that muscle paralysis induced by levamisole (sustained contraction), levamisole and tricaine (contraction and relaxation), or 2,3-Butanedione monoxime (BDM, muscle relaxation alone) dramatically reduced the percent fluorescence recovery of *mNG::fibulin* and the movement of *mNG::fibulin* ([Figure 5C](#); [Video S4](#);  $0.17 \pm 0.04 \mu\text{m/s}$  (control) versus  $0.08 \pm 0.02 \mu\text{m/s}$  levamisole,  $0.08 \pm 0.03 \mu\text{m/s}$  levamisole and tricaine,  $0.11 \pm 0.05 \mu\text{m/s}$  BDM,  $n = 5$  animals examined each,  $p < 0.01$  for each compared with control, Student's *t* test). These experiments indicate that the dynamic matrix components move non-directionally within the BM and that muscle contractions contribute to dynamic matrix mobility.

Finally, we examined how the more stable components recovered after photobleaching. Type XVIII collagen was the only stable BM protein that had detectable recovery within a 30-min window ( $\sim 10\%$ ), allowing for spatiotemporal FRAP analysis. In contrast to the more rapidly recovering components, we found that type XVIII collagen was recruited evenly throughout the pho-

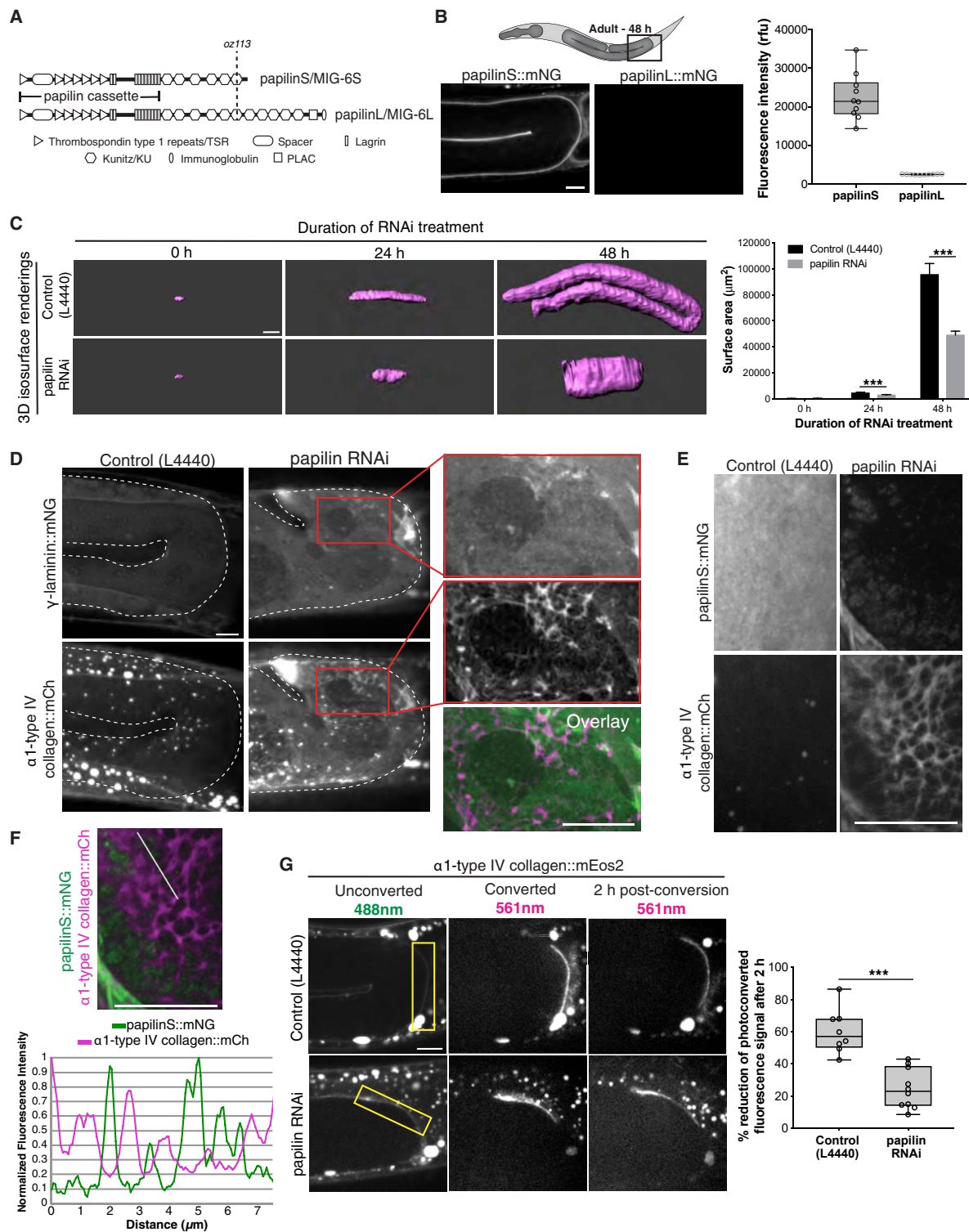
toleached region ([Figure 5B](#); [Video S1](#)), suggesting it is replaced by extracellular sources. Further, long term static imaging of recovering photobleached regions of type IV collagen, laminin, and papilinS did not reveal movement within the BM, suggesting they are also replaced by extracellular sources ([Figure S7D](#)). Taken together, these observations indicate that BMs are built on a stable laminin and collagen scaffold that includes type XVIII collagen and papilin within which other matrix proteins dynamically associate.

### Papilin/MIG-6 Promotes Removal of Type IV Collagen during BM Expansion

BM must expand during organ growth and in neoplastic diseases. Mechanisms that promote BM enlargement, and especially expansion of the stable collagen and laminin scaffolding, are unknown. We next used our collection of endogenously tagged BM components to examine BM enlargement in the gonad, which has a BM-encased surface area that increases more than 90-fold from hatching to early adulthood ([Jayadev et al., 2019](#)).

We focused on papilinS, which was present at levels exceeding all other matrix components combined at the initiation of gonadal BM expansion ([Figure 3B](#)). Papilin is a conserved proteoglycan that encodes at least two isoforms: one long (papilinL/MIG-6L) and one short (papilinS/MIG-6S; [Figure 6A](#)). We found that papilinL, which is secreted by the distal tip cells (DTCs) as they migrate, is present in the BM during gonad growth but at dramatically lower levels than papilinS ( $\sim 50$ -fold lower, [Figure 6B](#)). Genetic loss of papilinS is embryonic or early larval lethal ([Kawano et al., 2009](#)). We thus depleted both isoforms during gonad growth by feeding RNAi to L1-staged worms and analyzed laminin and collagen in gonadal BM of early adult animals (48 h post-hatching). Reduction of papilin perturbed gonad growth and BM expansion ([Figure 6C](#), more than 50% reduction in surface area compared with control animals) but did not result in BM dissolution or ruptures ( $n = 0/20$  animals with ruptured gonads observed), as occurs after RNAi-mediated loss of laminin or collagen ([Jayadev et al., 2019](#)). Instead, we found that papilin loss led to increased and fibrotic  $\alpha 1$ -type IV collagen::mNG compared with its smooth appearance in control animals (1.83-fold increase,  $n = 12$  animals,  $p < 0.0001$ , Student's *t* test). Notably, we saw the same fibrotic phenotype with  $\alpha 1$ -type IV collagen::mCherry ([Figure 6D](#)) ([Ihara et al., 2011](#)), which is tagged in a different location within  $\alpha 1$ -type IV collagen ([Figure S1](#);  $n = 10/10$  animals). In contrast, the smooth laminin network was unperturbed after papilin loss ([Figure 6D](#)), similar to controls ( $n = 10/10$ ). To assess if papilin was uniquely required during BM expansion, we initiated RNAi feeding at the L3 stage (24 h post-hatching, near the end of growth), 48-h adult (after growth), and 72-h adult (after growth) and found that type IV collagen was patterned normally 48 h after RNAi treatment in all cases ( $n = 8/8$  animals each), suggesting that papilin is not required for maintenance of collagen. We also examined animals harboring a mutant of papilin (*mig-6(oz113)*) that truncates the

(C) (Left) Confocal images (single z slices) of the L4 pharynx show differences in recovery rate of *mNG::fibulin* after photobleaching between control (polystyrene bead immobilization allowing muscle contractions) and tricaine/levamisole and BDM muscle paralysis treatments. Yellow arrows indicate the bleached half of the pharynx and dashed white box indicates the unbleached control region. (Right) Bar graph displays the mean recovery fraction at the end of the 15-min interval. Error bars denote standard error. All means were compared with the *mNG::fibulin* control ( $n = 5$  animals for each,  $**p < 0.001$ ,  $***p < 0.0001$ , Student's *t* test). Scale bar represents  $10 \mu\text{m}$ .



(legend on next page)

C-terminal domain of papilinL, leaving only the papilinS product (Figure 6A). These animals did not produce the type IV collagen fibrosis phenotype ( $n = 0/10$  animals), suggesting that domains unique to papilinL are not required for collagen remodeling during BM expansion.

To further understand the role of papilin during BM growth, we analyzed RNAi-mediated loss of papilinS protein and the patterning of type IV collagen. We found that after L1 RNAi-initiated loss of papilin, the papilinS protein declined dramatically but was still present in a patchy, punctate pattern in the gonads of 48-h young adult animals (Figure 6E). The localization of this residual papilinS correlated with areas where the type IV collagen was smoothly patterned, whereas regions of papilin absence was where collagen levels were increased and fibrotic (Figures 6E and 6F). To examine how papilin regulates type IV collagen during BM growth, we generated an  $\alpha 1$ -type IV collagen::mEos2 knockin strain (Figure S1). mEos2 is a highly stable photoconvertible fluorophore that converts from green to red with ultraviolet light (McKinney et al., 2009). Optical highlighting of  $\alpha 1$ -type IV collagen::mEos2 within the BM of the gonad in 48-h young adults revealed a ~60% loss of photoconverted collagen signal after 2 h in control animals but only a ~20% reduction in papilin RNAi treated animals (Figure 6G). Taken together, these results indicate that papilin plays a localized role in mediating type IV collagen removal during BM expansion, which likely accounts for the buildup of BM collagen after papilin loss.

### Papilin Limits BM Association of Collagen-Modifying ADAMTS Proteases and Peroxidase-2

Papilins are structurally similar to ADAMTS matrix-associated metalloproteinases and share a papilin cassette (thrombospondin type-1 repeats [TSR] with a spacer sequence rich in cysteine residues) but lack a catalytic domain (Figure 6A). *Drosophila* papilin can bind to and inhibit a vertebrate procollagen N-protease ADAMTS *in vitro* (Kramerova et al., 2000). Studies with dominant papilin *mig-6* alleles have suggested they may regulate the localization or the activity of ADAMTS protease MIG-17 to control the path of DTC migration (Kawano et al., 2009).

As our data indicated that papilin promotes type IV collagen removal, we first depleted the five *C. elegans* ADAMTS prote-

ases—*adt-1*, *adt-2*, *adt-3*, *gon-1*, and *mig-17*—by RNAi at the L1 stage to determine if loss of any phenocopied papilin loss. Reduction of these ADAMTS proteases, however, did not lead to a buildup of type IV collagen ( $n > 10$  animals for each), suggesting that papilin does not promote ADAMTS proteases activity to regulate collagen removal. We next examined whether papilin might inhibit an ADAMTS protease and co-depleted papilin in combination with each of the five ADAMTS proteases to see if loss of any suppressed the cobweb collagen buildup. Strikingly, reduction of *gon-1* in combination with papilin restored smooth collagen patterning ( $n = 21/23$  rescued versus  $0/16$  papilin RNAi alone,  $n > 10$  animals for each ADAMTS; Figure 7A). To examine the localization of GON-1, an ortholog to vertebrate ADAMTS9 (Clay and Sherwood, 2015), we generated a knockin strain (GON-1::mNG; Figure S2) and found that reduction of papilin led to a significant increase in ADAMTS9/GON-1 associated with the gonadal BM (Figure 7B). MIG-17::mNG levels were similarly increased in the BM after papilin loss (Figure 7B). We also examined two additional type IV collagen-modifying enzymes—peroxidase-1 and peroxidase-2. Peroxidase-2 mediates covalent sulfilimine bond formation between type IV collagen molecules, while peroxidase-1 antagonizes peroxidase-2 activity (Gotenstein et al., 2010). Loss of papilin led to increased levels of peroxidase-2 within the BM, but not peroxidase-1 (Figure 7B). RNAi-mediated reduction of peroxidase-2 in combination with papilin, however, did not suppress the collagen phenotype resulting from papilin loss ( $n = 15/15$  animals had fibrotic collagen). Collectively, these observations indicate that papilin plays a localized role in limiting BM access (and perhaps activity) of ADAMTS9/GON-1 to promote collagen removal and exerts a similar influence on the localization of the ADAMTS protease MIG-17 and the peroxidase-2 enzyme. Thus, papilin might play a broad role in collagen remodeling during BM growth.

### DISCUSSION

A major challenge in BM biology is examining the dynamics and regulation of these dense, varied, and complex matrices *in vivo* (Hohenester and Yurchenco, 2013). Live antibody labeling of laminin and type IV collagen in *ex vivo* cultures in mice

### Figure 6. Papilin Promotes Type IV Collagen Network Remodeling during BM Growth

(A) A diagram of papilin/MIG-6 shows the protein domains of papilinS and papilinL isoforms and the papilinL truncation mutant (*mig-6(oz113)*). (B) (Top left) A diagram of the *C. elegans* gonad (gray) where levels of papilinS::mNG and papilinL::mNG fluorescence were compared (black box). (Bottom left) Single confocal z slices of papilinS::mNG and papilinL::mNG at the young adult stage and (right) quantification of fluorescence (boxplot,  $n = 10$  animals for each). (C) (Left) 3D isosurface renderings of gonadal  $\alpha 1$ -type IV collagen::mCh following 0, 24, or 48 h of RNAi treatment in control and papilin RNAi animals. (Right) Quantification of gonadal surface area; bar graphs show mean surface area and error bars represent standard deviation ( $n = 3-6$  animals examined for each, \*\*\* $p < 0.0001$ , Student's *t* test). (D) Confocal maximum intensity projections show co-localization of  $\gamma$ -laminin::mNG and  $\alpha 1$ -type IV collagen::mCh in the turn region of the adult gonad in an untreated control and a papilin RNAi knockdown animal. Reduction of papilin disrupted gonad growth and led to a fibrous increase in type IV collagen. The laminin network in the same animal was normal (magnified insets with overlay,  $n = 10$  animals). (E) Maximum intensity projections show co-localization of the even distribution of papilinS::mNG and  $\alpha 1$ -type IV collagen::mCh within control animals BM compared with the patchy localization of papilinS and fibrous  $\alpha 1$ -type IV collagen::mCh after RNAi-mediated loss of papilin. (F) Overlay of residual papilinS::mNG and  $\alpha 1$ -type IV collagen::mCh maximum intensity projection images after RNAi knockdown of papilin. A line plot indicated by the white line shows that areas with low papilin have high type IV collagen and vice versa ( $n = 5/5$  animals). (G) (Left) Single confocal z slices of  $\alpha 1$ -type IV collagen::mEos2 prior to, immediately after, and 2 h after photoconversion in a control and papilin RNAi knockdown animal. Optically highlighted  $\alpha 1$ -type IV collagen::mEos2 is indicated by yellow boxes. (Right) Quantification of the percentage reduction in mean photoconverted (red) mEos2 signal after 2 h (boxplot,  $n = 8-10$  animals for each, \*\*\* $p < 0.0001$ , Student's *t* test). Scale bars represent 10  $\mu\text{m}$  except (C), which is 25  $\mu\text{m}$ .

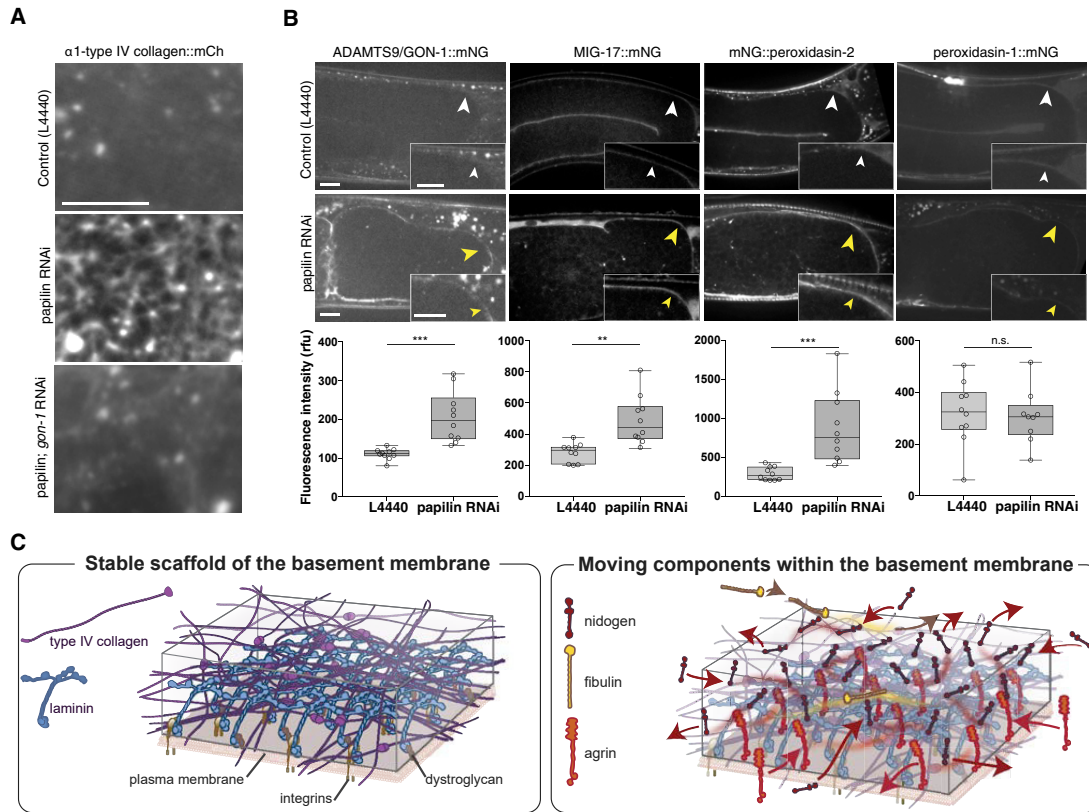


**Figure 7. Papilin Limits ADAMTS Protease and Peroxidase-2 Gonadal BM Association**

(A) Confocal sum projections of  $\alpha 1$ -type IV collagen::mCh fluorescence in the gonadal BM. RNAi knockdown of papilin led to an increased fibrous type IV collagen network ( $n = 16/16$ ) that was rescued by loss of *gon-1* ( $n = 21/23$ ).

(B) (Top) Single confocal slices through the gonad arm shows GON-1::mNG, MIG-17::mNG, mNG::peroxidase-2, and peroxidase-1::mNG in control or papilin RNAi treated animals. Loss of papilin resulted in increased BM association of GON-1, MIG-17, and peroxidase-2, but not peroxidase-1. (Bottom) Quantification of BM fluorescence intensity (boxplot, control  $n = 10$  and papilin RNAi  $n = 10$  for each, n.s., not significant,  $^{**}p < 0.001$  or  $^{***}p < 0.0001$ , Student's *t* test). Scale bars represent 10  $\mu$ m.

(C) A model for BM dynamics. (Left) Laminin (and possibly type IV collagen, Jayadev et al., 2019) associate with the cell membranes through integrin and dystroglycan receptors forming a stable scaffolding. (Right) Nidogen, fibulin, and agrin (spondin and peroxidase-1 not shown) move dynamically within the laminin and type IV collagen network.

(Harunaga et al., 2014; Pflücke and Sixt, 2009) and a type I collagen-GFP that localizes adjacent to BMs in zebrafish (van den Berg et al., 2019) have provided insights into BM dynamics during cell migrations and glandular morphogenesis. However, no BM components have been tagged with a genetically encoded fluorophore in a vertebrate to directly follow BM dynamics. In *Drosophila*, GFP-tagged transgenes expressing laminin and nidogen, and GFP inserted via exon traps into type IV collagen and perlecan genes, have revealed their regulation and functions during BM deposition, signaling, tissue shaping, and wound healing (Isabella and Horne-Badovinac, 2016; Ma et al., 2017; Matsubayashi et al., 2017; Ramos-Lewis et al., 2018). *Drosophila* studies, however, have not endogenously tagged most BM components, and live imaging of BMs after embryogenesis has only been achieved using dissected tissues (Cetera et al., 2016). To overcome these limitations, we extended our previous studies of endogenous mNG-tagged  $\gamma$ -laminin, dystroglycan, and  $\alpha$ - and  $\beta$ -integrins (Jayadev

et al., 2019; Naegeli et al., 2017) to complete a comprehensive assembly of endogenously tagged BM components with 17 tagged BM matrix components and 12 tagged receptors. In addition, this evolving collection includes type IV collagen tagged with the photoconvertible fluorophore mEos2 and two BM-localized ADAMTS proteases—ADAMTS9/GON-1 (this study) and MIG-17 (Ji et al., 2019). Importantly, most of these BM components have strong loss-of-function phenotypes, including embryonic or larval lethality (laminin, type IV collagen, spondin, papilin, teneurin, perlecan, SPARC, and integrin) and sterility or low brood size (fibulin, hemicentin, dystroglycan, and ADAMTS9) (Kawano et al., 2009; Kramer, 2005; Kramerova et al., 2000; Muriel et al., 2005; Trzebiatowska et al., 2008; Vogel and Hedgecock, 2001; Woo et al., 2008). The normal health of the genome-edited strains, the tight association of the tagged proteins with BMs, and the presence of full-length protein products provide strong evidence that the tagged proteins show endogenous regulation and localization.



Although BMs in adult tissues are remarkably diverse, it is unknown when during development this diversity arises. Work on the initial formation of BMs in mice, *C. elegans*, and *Drosophila* embryos has established that laminin deposition occurs early and is required for BM assembly (Hohenester and Yurchenco, 2013; Kao et al., 2006; Matsubayashi et al., 2017; Urbano et al., 2009). In *C. elegans*, laminin is deposited and BMs start forming near the end of gastrulation (Huang et al., 2003). We found that in addition to laminin, nidogen and papilin were present on all BMs at this time, suggesting these components form an initiating BM template. Notably, at this nascent phase, distinct forms of laminin and papilin had tissue-specific BM localization. Further, the collagen cross-linking enzyme peroxidasin-2 and the integrin receptor PAT-2/PAT-3 were restricted to muscle BMs. Thus, BMs have a common early template, but tissue-specific differences are also present. As development proceeded, BM complexity and heterogeneity between tissues increased and gradients and regionally increased concentrations of matrix components appeared. In the L1-stage pharynx BM, type IV collagen was found in a gradient, while components like type XVIII collagen and spondin were strongly enriched in specific pharynx sub-regions. A gradient of GFP-tagged type IV collagen has also been observed in the *Drosophila* egg chamber BM, where it translates into a stiffness gradient that elongates the egg chamber (Crest et al., 2017). Local differences and gradients in BM components are likely common, but overlooked features of BMs that have important roles during organ formation and function.

How BMs increase in size during organ growth in development, regeneration, and tumor expansion is a crucial but unknown aspect of BM regulation. Using our ability to compare fluorescence and therefore BM protein levels, we found that papilinS was present at higher levels than all other BM components combined in the L1-stage gonad—an organ where the BM will enlarge more than 90-fold during subsequent development (Jayadev et al., 2019). We found that loss of papilin limited BM expansion and perturbed gonad growth, suggesting an important role for papilin in BM enlargement. RNAi-mediated depletion of papilin during gonad growth revealed that in BM areas where papilinS protein was no longer detectable, the collagen scaffold was increased in levels and fibrous. In contrast, laminin retained its uniform localization after papilin loss. Optical highlighting of a photoconvertible type IV collagen showed that the collagen was more stably associated with the BM after papilin reduction, indicating that papilin promotes type IV collagen removal from BMs during gonad growth, which may account for its function in facilitating BM expansion and tissue growth. Papilins have structural similarities to ADAMTS-secreted matrix-associated metalloproteinases, but they lack a proteolytic catalytic site. *In vitro* studies have shown that *Drosophila* papilin binds to and inhibits the activity of a vertebrate procollagen N-proteinase ADAMTS (Kramerova et al., 2000). Our studies suggest that in addition to directly inhibiting ADAMTS proteases, papilin also limits the BM association of ADAMTS proteins. Loss of papilin led to a significant increase in the BM association of the ADAMTS proteinases GON-1 and MIG-17 as well as the type IV collagen cross-linking enzyme peroxidasin-2. Supporting a possible functional role for papilin's exclusion of these enzymes, we found that reduction of *gon-1* in combination with

papilin partially rescued the normal patterning of type IV collagen on the gonad BM. Although it might seem counterintuitive that loss of an ADAMTS protease reduces collagen buildup and fibrotic appearance in the gonadal BM, a number of human ADAMTS proteins are pro-fibrotic and associated with increased ECM deposition (Perrucci et al., 2018). Aggrecan and versican are the only characterized substrates for ADAMTS9 (Kelwick et al., 2015), the vertebrate GON-1 ortholog; however, these proteoglycans are not present in *C. elegans*. Thus, GON-1 (and ADAMTS9) likely has an additional substrate(s) that regulates type IV collagen removal from BMs.

No studies have yet assessed the dynamics of BM components within BMs after deposition. By performing FRAP experiments on the mNG-tagged matrix proteins, we found that laminin and type IV collagen, the two central scaffolding components of BM, are stable and have slow recovery times, on the order of many hours. Papilin and type XVIII collagen also displayed slow recovery after photobleaching. These slow recovery rates may reflect the normal degradation and replacement rates of these proteins during development. All other matrix components that were assessed—fibulin, nidogen, agrin, peroxidasin-1, and spondin—showed rapid recovery of bleached regions on the order of minutes. We considered that these BM components might be rapidly exchanging between the BM and the extracellular fluid. However, fluorescence recovery did not occur evenly along the bleached region of BM. Instead, recovery occurred first at the edge of the photobleached region, indicating that BM components predominantly recover by moving within the more stable scaffolding components. We also found that this movement was non-directional and in the case of the mobile component fibulin, was enhanced by muscle contractions. Together, these observations provide a new model for BM dynamics, where a relatively stable scaffolding of laminin and type IV collagen hosts more dynamic regulatory components that move within this scaffolding (Figure 7C; Video S5). We suspect that the more dynamic components have numerous weak interactions with other BM components, which not only maintain their association with the BM but also allow for their movement. Consistent with this, nidogen has many BM-binding partners, including laminin, type IV collagen, and perlecan (Yurchenco, 2011). Fibulins also associate with many other BM proteins (Kobayashi et al., 2007). The mobile matrix components might allow BMs to dynamically respond to mechanical changes in tissues, particularly as the mobility of fibulin is affected by the mechanical activity of muscle contraction. Further, as growth factors can bind to agrin and fibulin (Bányai et al., 2010; Fresco et al., 2016), mobile matrix components may serve as conduits for growth factor trafficking.

We have shown here that we can examine BM emergence, growth, composition, and dynamics with our comprehensive collection of endogenously tagged BM components. We envision future studies engineering disease-associated mutations into these strains to probe how these mutations affect BM component trafficking, localization, and dynamics. In addition, studies can now be conducted in combination with FRAP and photoconversion to identify genes mediating the turnover of the stable collagen and laminin scaffoldings—networks that accumulate in fibrosis, diabetes, aging, and tissue decline (Candiello et al., 2010; Mak and Mei, 2017; Tsiibary, 2003). Thus, the

use of these endogenously tagged BM components is poised to further deepen our understanding of this ancient and fascinating animal ECM.

## STAR★METHODS

Detailed methods are provided in the online version of this paper and include the following:

- **KEY RESOURCES TABLE**
- **RESOURCE AVAILABILITY**
  - Lead Contact
  - Materials Availability
  - Data and Code Availability
- **EXPERIMENTAL MODEL AND SUBJECT DETAILS**
  - Worm Handling and Strains
- **METHOD DETAILS**
  - CRISPR Strain Construction
  - CRISPR Strain Viability Analysis
  - Fusion Protein Localization and Cleavage Analysis
  - Fusion Protein Western Blot Analysis
  - RNA Interference
  - ATP Depletion and Muscle Paralysis
  - Imaging
  - Generation of Model BM Proteins and Receptors for Schematics
- **QUANTIFICATION AND STATISTICAL ANALYSIS**
  - BM Composition Comparisons
  - FRAP Analysis
  - Photoconversion Analysis
  - Protein Movement Imaging
  - Papilin Isoform Intensity Comparison
  - RNAi Knockdown Efficiency
  - Scoring of Papilin Knockdown Phenotype
  - Quantification of ADAMTS Localization Following Papilin Knockdown
  - Statistical Analysis

## SUPPLEMENTAL INFORMATION

Supplemental Information can be found online at <https://doi.org/10.1016/j.devcel.2020.05.022>.

## ACKNOWLEDGMENTS

We thank Lisa Cameron of the Duke University LMCF for imaging advice, M. Clay for helpful discussions, and K. Gordon for comments on the manuscript. We thank A. Kawska (info@illuscintia) for her work on schematics and H. Bue-low for advice on *sdn-1* tagging. E.H. is supported by 129351-PF-16-024-01-CSM from American Cancer Society, S.G.P. by F31 HD097901, L.C.K. by F32GM103148, and S.G.P. and D.R.S. by R35GM118049 and R21HD084290. Some strains were provided by the Caenorhabditis Genetics Center, which is funded by NIH Office of Research Infrastructure Programs (P40 OD010440).

## AUTHOR CONTRIBUTIONS

Conceptualization, D.P.K. and D.R.S.; Methodology, D.P.K., E.H., R.J., L.C.K., Q.C., B.D.H., and D.R.S.; Investigation, D.P.K., E.H., R.J., L.C.K., Q.C., J.L.J., D.R.S., and S.G.P.; Writing – Original Draft, D.P.K. and D.R.S.; Writing – Review & Editing, D.P.K., D.R.S., E.H., R.J., L.C.K., S.G.P., and B.D.H.; Visualiza-

tion, D.P.K., E.H., and R.J.; Funding Acquisition, D.R.S.; Resources, D.R.S.; Supervision, D.R.S.

## DECLARATION OF INTERESTS

The authors declare no competing interests.

Received: December 5, 2019

Revised: March 9, 2020

Accepted: May 15, 2020

Published: June 24, 2020

## REFERENCES

- Bajic, G., Yattine, L., Klos, A., and Andersen, G.R. (2013). Human C3a and C3a desArg anaphylatoxins have conserved structures, in contrast to C5a and C5a desArg. *Protein Sci.* 22, 204–212.
- Bányai, L., Sonderegger, P., and Patthy, L. (2010). Agrin binds BMP2, BMP4 and TGFβ1. *PLoS One* 5, e10758.
- Bunt, S., Hooley, C., Hu, N., Scallan, C., Weavers, H., and Skaer, H. (2010). Hemocyte-secreted type IV collagen enhances BMP signaling to guide renal tubule morphogenesis in *Drosophila*. *Dev. Cell* 19, 296–306.
- Candiello, J., Cole, G.J., and Halfter, W. (2010). Age-dependent changes in the structure, composition and biophysical properties of a human basement membrane. *Matrix Biol.* 29, 402–410.
- Carafoli, F., Hussain, S.A., and Hohenester, E. (2012). Crystal structures of the network-forming short-arm tips of the laminin β1 and γ1 chains. *PLoS One* 7, e42473.
- Cetera, M., Lewellyn, L., and Horne-Badovinac, S. (2016). Cultivation and live imaging of *drosophila* ovaries. *Methods Mol. Biol.* 1478, 215–226.
- Chang, J., and Chaudhuri, O. (2019). Beyond proteases: basement membrane mechanics and cancer invasion. *J. Cell Biol.* 218, 2456–2469.
- Clay, M.R., and Sherwood, D.R. (2015). Basement membranes in the worm: a dynamic scaffolding that instructs cellular behaviors and shapes tissues. *Curr. Top. Membr.* 76, 337–371.
- Crest, J., Diz-Muñoz, A., Chen, D.Y., Fletcher, D.A., and Bilder, D. (2017). Organ sculpting by patterned extracellular matrix stiffness. *eLife* 6, e24958.
- Decaris, M.L., Gatmaitan, M., FlorCruz, S., Luo, F., Li, K., Holmes, W.E., Hellerstein, M.K., Turner, S.M., and Emson, C.L. (2014). Proteomic analysis of altered extracellular matrix turnover in bleomycin-induced pulmonary fibrosis. *Mol. Cell. Proteomics* 13, 1741–1752.
- Dickinson, D.J., and Goldstein, B. (2016). CRISPR-based methods for *Caenorhabditis elegans* genome engineering. *Genetics* 202, 885–901.
- Edelstein, A., Amodaj, N., Hoover, K., Vale, R., and Stuurman, N. (2010). Computer control of microscopes using μManager. *Curr. Protoc. Mol. Biol.* 92, 14.20.1–14.20.17.
- Edelstein, A.D., Tsuchida, M.A., Amodaj, N., Pinkard, H., Vale, R.D., and Stuurman, N. (2014). Advanced methods of microscope control using μManager software. *J. Biol. Methods* 7, e10.
- Fidler, A.L., Boudko, S.P., Rokas, A., and Hudson, B.G. (2018). The triple helix of collagens - an ancient protein structure that enabled animal multicellularity and tissue evolution. *J. Cell Sci.* 131, jcs203950.
- Fresco, V.M., Kern, C.B., Mohammadi, M., and Tsal, W.O. (2016). Fibulin-1 binds to fibroblast growth factor 8 with high affinity: effects on embryo survival. *J. Biol. Chem.* 291, 18730–18739.
- Gotenstein, J.R., Swale, R.E., Fukuda, T., Wu, Z., Giurumescu, C.A., Goncharov, A., Jin, Y., and Chisholm, A.D. (2010). The *C. elegans* peroxidase PXX-2 is essential for embryonic morphogenesis and inhibits adult axon regeneration. *Development* 137, 3603–3613.
- Graham, P.L., Johnson, J.J., Wang, S., Sibley, M.H., Gupta, M.C., and Kramer, J.M. (1997). Type IV collagen is detectable in most, but not all, basement membranes of *Caenorhabditis elegans* and assembles on tissues that do not express it. *J. Cell Biol.* 137, 1171–1183.
- Halfter, W., Moes, S., Asgeirsson, D.O., Halfter, K., Oertle, P., Melo Herraiz, E., Plodinec, M., Jenoe, P., and Henrich, P.B. (2017). Diabetes-related changes in

the protein composition and the biomechanical properties of human retinal vascular basement membranes. *PLoS One* 12, e0189857.

Hall, D.H., Herndon, L.A., and Altun, Z. (2017). Introduction to *C. elegans* embryo anatomy. In *WormAtlas* (Cold Spring Harbor Laboratory Press). <https://doi.org/10.3908/wormatlas.4.1>.

Harunaga, J.S., Doyle, A.D., and Yamada, K.M. (2014). Local and global dynamics of the basement membrane during branching morphogenesis require protease activity and actomyosin contractility. *Dev. Biol.* 394, 197–205.

Heppert, J.K., Dickinson, D.J., Pani, A.M., Higgins, C.D., Steward, A., Ahninger, J., Kuhn, J.R., and Goldstein, B. (2016). Comparative assessment of fluorescent proteins for in vivo imaging in an animal model system. *Mol. Biol. Cell* 27, 3385–3394.

Hesselson, D., and Kimble, J. (2006). Growth control by EGF repeats of the *C. elegans* fibulin-1C isoform. *J. Cell Biol.* 175, 217–223.

Hohenester, E., and Yurchenco, P.D. (2013). Laminins in basement membrane assembly. *Cell Adh. Migr.* 7, 56–63.

Hong, S., and Pedersen, P.L. (2008). ATP synthase and the actions of inhibitors utilized to study its roles in human health, disease, and other scientific areas. *Microbiol. Mol. Biol. Rev.* 72, 590–641.

Hopf, M., Göhring, W., Ries, A., Timpl, R., and Hohenester, E. (2001). Crystal structure and mutational analysis of a perlecan-binding fragment of nidogen-1. *Nat. Struct. Biol.* 8, 634–640.

Hrus, A., Lau, G., Hutter, H., Schenk, S., Ferralli, J., Brown-Luedi, M., Chiquet-Ehrismann, R., and Canevascini, S. (2007). *C. elegans* agrin is expressed in pharynx, IL1 neurons and distal tip cells and does not genetically interact with genes involved in synaptogenesis or muscle function. *PLoS One* 2, e731.

Huang, C.C., Hall, D.H., Hedgecock, E.M., Kao, G., Karantza, V., Vogel, B.E., Hutter, H., Chisholm, A.D., Yurchenco, P.D., and Wadsworth, W.G. (2003). Laminin alpha subunits and their role in *C. elegans* development. *Development* 130, 3343–3358.

Hussain, S.A., Carafoli, F., and Hohenester, E. (2011). Determinants of laminin polymerization revealed by the structure of the  $\alpha 5$  chain amino-terminal region. *EMBO Rep.* 12, 276–282.

Ihara, S., Hagedorn, E.J., Morrissey, M.A., Chi, Q., Motegi, F., Kramer, J.M., and Sherwood, D.R. (2011). Basement membrane sliding and targeted adhesion remodels tissue boundaries during uterine-vulval attachment in *Caenorhabditis elegans*. *Nat. Cell Biol.* 13, 641–651.

Isabella, A.J., and Horne-Badovinac, S. (2016). Rab10-mediated secretion synergizes with tissue movement to build a polarized basement membrane architecture for organ morphogenesis. *Dev. Cell* 38, 47–60.

Jayadev, R., Chi, Q., Keeley, D.P., Hastie, E.L., Kelley, L.C., and Sherwood, D.R. (2019).  $\alpha$ -integrins dictate distinct modes of type IV collagen recruitment to basement membranes. *J. Cell Biol.* 218, 3098–3116.

Ji, T., Wang, K., Fan, J., Huang, J., Wang, M., Dong, X., Shi, Y., Manning, L., Zhang, X., Shao, Z., and Colón-Ramos, D.A. (2019). ADAMTS-family protease MiG-17 regulates synaptic allometry by modifying the extracellular matrix and modulating glia morphology during growth. *bioRxiv*. <https://doi.org/10.1101/734830v1>.

Kamath, R.S., Fraser, A.G., Dong, Y., Poulin, G., Durbin, R., Gotta, M., Kanapin, A., Le Bot, N., Moreno, S., Sohrmann, M., et al. (2003). Systematic functional analysis of the *Caenorhabditis elegans* genome using RNAi. *Nature* 421, 231–237.

Kao, G., Huang, C.C., Hedgecock, E.M., Hall, D.H., and Wadsworth, W.G. (2006). The role of the laminin beta subunit in laminin heterotrimer assembly and basement membrane function and development in *C. elegans*. *Dev. Biol.* 290, 211–219.

Kawano, T., Zheng, H., Merz, D.C., Kohara, Y., Tamai, K.K., Nishiwaki, K., and Culotti, J.G. (2009). *C. elegans* mig-6 encodes papilin isoforms that affect distinct aspects of DTC migration, and interacts genetically with MiG-17 and collagen IV. *Development* 136, 1433–1442.

Kelwick, R., Desanlis, I., Wheeler, G.N., and Edwards, D.R. (2015). The ADAMTS (a disintegrin and metalloproteinase with thrombospondin motifs) family. *Genome Biol* 16, 113.

Kobayashi, N., Kostka, G., Garbe, J.H.O., Keene, D.R., Bächinger, H.P., Hanisch, F.G., Markova, D., Tsuda, T., Timpl, R., Chu, M.L., and Sasaki, T. (2007). A comparative analysis of the fibulin protein family. Biochemical characterization, binding interactions, and tissue localization. *J. Biol. Chem.* 282, 11805–11816.

Kramer, J.M. (2005). Basement membranes. *WormBook* (Cold Spring Harbor Laboratory Press), pp. 1–15.

Kramerova, I.A., Kawaguchi, N., Fessler, L.I., Nelson, R.E., Chen, Y., Kramerov, A.A., Kusche-Gullberg, M., Kramer, J.M., Ackley, B.D., Sieron, A.L., et al. (2000). Papilin in development; a pericellular protein with a homology to the ADAMTS metalloproteinases. *Development* 127, 5475–5485.

Kvansakul, M., Hopf, M., Ries, A., Timpl, R., and Hohenester, E. (2001). Structural basis for the high-affinity interaction of nidogen-1 with immunoglobulin-like domain 3 of perlecan. *EMBO J.* 20, 5342–5346.

Li, S., Qi, Y., McKee, K., Liu, J., Hsu, J., and Yurchenco, P.D. (2017). Integrin and dystroglycan compensate each other to mediate laminin-dependent basement membrane assembly and epiblast polarization. *Matrix Biol.* 57–58, 272–284.

Lössl, P., Köbel, K., Tänzler, D., Nannemann, D., Ihling, C.H., Keller, M.V., Schneider, M., Zaucke, F., Meiler, J., and Sinz, A. (2014). Analysis of nidogen-1/laminin  $\gamma 1$  interaction by cross-linking, mass spectrometry, and computational modeling reveals multiple binding modes. *PLoS One* 9, e112886.

Ma, M., Cao, X., Dai, J., and Pastor-Pareja, J.C. (2017). Basement membrane manipulation in drosophila wing discs affects dpp retention but not growth mechanoregulation. *Dev. Cell* 42, 97–106.e4.

Mak, K.M., and Mei, R. (2017). Basement membrane type IV collagen and laminin: an overview of their biology and value as fibrosis biomarkers of liver disease. *Anat. Rec. (Hoboken)* 300, 1371–1390.

Mango, S.E. (2007). The *C. elegans* pharynx: a model for organogenesis. *WormBook* (Cold Spring Harbor Laboratory Press), pp. 1–26.

Matsubayashi, Y., Louani, A., Dragu, A., Sánchez-Sánchez, B.J., Serna-Morales, E., Yolland, L., Gyoergy, A., Vizcay, G., Fleck, R.A., Heddleston, J.M., et al. (2017). A moving source of matrix components is essential for de novo basement membrane formation. *Curr. Biol.* 27, 3526–3534.e4.

Matsuo, K., Koga, A., and Ihara, S. (2019). Visualization of endogenous NID-1 and EMB-9 in *C. elegans*. *MicroPublication Biol.* <https://doi.org/10.17912/micropub.biology.000110>.

McCoy, J.C., Walker, R.G., Murray, N.H., and Thompson, T.B. (2019). Crystal structure of the WFIKN2 follistatin domain reveals insight into how it inhibits growth differentiation factor 8 (GDF8) and GDF11. *J. Biol. Chem.* 294, 6333–6343.

McKinney, S.A., Murphy, C.S., Hazelwood, K.L., Davidson, M.W., and Looger, L.L. (2009). A bright and photostable photoconvertible fluorescent protein. *Nat. Methods* 6, 131–133.

Moran, T., Gat, Y., and Fass, D. (2015). Laminin L4 domain structure resembles adhesion modules in ephrin receptor and other transmembrane glycoproteins. *FEBS J.* 282, 2746–2757.

Morin, X., Daneman, R., Zavortink, M., and Chia, W. (2001). A protein trap strategy to detect GFP-tagged proteins expressed from their endogenous loci in *Drosophila*. *Proc. Natl. Acad. Sci. USA* 98, 15050–15055.

Morrissey, M.A., Jayadev, R., Miley, G.R., Blebea, C.A., Chi, Q., Ihara, S., and Sherwood, D.R. (2016). SPARC promotes cell invasion in vivo by decreasing type IV collagen levels in the basement membrane. *PLoS Genet.* 12, e1005905.

Morrissey, M.A., and Sherwood, D.R. (2015). An active role for basement membrane assembly and modification in tissue sculpting. *J. Cell Sci.* 128, 1661–1668.

Muriel, J.M., Dong, C., Hutter, H., and Vogel, B.E. (2005). Fibulin-1C and fibulin-1D splice variants have distinct functions and assemble in a hemiscitin-dependent manner. *Development* 132, 4223–4234.

Naba, A., Clauser, K.R., Lamar, J.M., Carr, S.A., and Hynes, R.O. (2014). Extracellular matrix signatures of human mammary carcinoma identify novel metastasis promoters. *eLife* 3, e01308.

Naegeli, K.M., Hastie, E., Garde, A., Wang, Z., Keeley, D.P., Gordon, K.L., Pani, A.M., Kelley, L.C., Morrissey, M.A., Chi, Q., et al. (2017). Cell invasion in vivo via rapid exocytosis of a transient lysosome-derived membrane domain. *Dev. Cell* 43, 403–417.e10.

Nyström, A., Bornert, O., and Kühl, T. (2017). Cell therapy for basement membrane-linked diseases. *Matrix Biol.* 57–58, 124–139, 124–139.

Perrucci, G.L., Rurali, E., and Pompilio, G. (2018). Cardiac fibrosis in regenerative medicine: destroy to rebuild. *J. Thorac. Dis.* 10, S2376–S2389.

Petzold, B.C., Park, S.J., Ponce, P., Roozeboom, C., Powell, C., Goodman, M.B., and Pruitt, B.L. (2011). *Caenorhabditis elegans* body mechanics are regulated by body wall muscle tone. *Biophys. J.* 100, 1977–1985.

Pflicke, H., and Sixt, M. (2009). Preformed portals facilitate dendritic cell entry into afferent lymphatic vessels. *J. Exp. Med.* 206, 2925–2935.

Pöschl, E., Schlötzer-Schrehardt, U., Brachvogel, B., Saito, K., Ninomiya, Y., and Mayer, U. (2004). Collagen IV is essential for basement membrane stability but dispensable for initiation of its assembly during early development. *Development* 131, 1619–1628.

Ramos-Lewis, W., LaFever, K.S., and Page-McCaw, A. (2018). A scar-like lesion is apparent in basement membrane after wound repair in vivo. *Matrix Biol.* 74, 101–120.

Randles, M.J., Humphries, M.J., and Lennon, R. (2017). Proteomic definitions of basement membrane composition in health and disease. *Matrix Biol.* 57–58, 12–28.

Rasmussen, J.P., Reddy, S.S., and Priess, J.R. (2012). Laminin is required to orient epithelial polarity in the *C. elegans* pharynx. *Development* 139, 2050–2060.

Rogers, R.S., and Nishimune, H. (2017). The role of laminins in the organization and function of neuromuscular junctions. *Matrix Biol.* 57–58, 86–105, 86–105.

Rual, J.F., Ceron, J., Koreth, J., Hao, T., Nicot, A.S., Hirozane-Kishikawa, T., Vandenhaute, J., Orkin, S.H., Hill, D.E., van den Heuvel, S., and Vidal, M. (2004). Toward improving *Caenorhabditis elegans* phenome mapping with an ORFeome-based RNAi library. *Genome Res.* 14, 2162–2168.

Schiller, H.B., Fernandez, I.E., Burgstaller, G., Schaab, C., Scheltema, R.A., Schwarzmayr, T., Strom, T.M., Eickelberg, O., and Mann, M. (2015). Time- and compartment-resolved proteome profiling of the extracellular niche in lung injury and repair. *Mol. Syst. Biol.* 11, 819.

Schindelin, J., Arganda-Carreras, I., Frise, E., Kaynig, V., Longair, M., Pietzsch, T., Preibisch, S., Rueden, C., Saalfeld, S., Schmid, B., et al. (2012). Fiji: an open-source platform for biological-image analysis. *Nat. Methods* 9, 676–682.

Sherwood, D.R., Butler, J.A., Kramer, J.M., and Sternberg, P.W. (2005). FOS-1 promotes basement-membrane removal during anchor-cell invasion in *C. elegans*. *Cell* 121, 951–962.

Smyth, N., Vatansever, H.S., Murray, P., Meyer, M., Frie, C., Paulsson, M., and Edgar, D. (1999). Absence of basement membranes after targeting the LAMC1 gene results in embryonic lethality due to failure of endoderm differentiation. *J. Cell Biol.* 144, 151–160.

Stetefeld, J., Alexandrescu, A.T., Maciejewski, M.W., Jenny, M., Rathgeb-Szabo, K., Schulthess, T., Landwehr, R., Frank, S., Ruegg, M.A., and Kammerer, R.A. (2004). Modulation of agrin function by alternative splicing and Ca<sup>2+</sup> binding. *Structure* 12, 503–515.

Stetefeld, J., Mayer, U., Timpl, R., and Huber, R. (1996). Crystal structure of three consecutive laminin-type epidermal growth factor-like (LE) modules of laminin gamma1 chain harboring the nidogen binding site. *J. Mol. Biol.* 257, 644–657.

Takagi, J., Yang, Y., Liu, J.H., Wang, J.H., and Springer, T.A. (2003). Complex between nidogen and laminin fragments reveals a paradigmatic beta-propeller interface. *Nature* 424, 969–974.

Topf, U., and Chiquet-Ehrismann, R. (2011). Genetic interaction between *Caenorhabditis elegans* teneurin ten-1 and prolyl 4-hydroxylase phy-1 and their function in collagen IV-mediated basement membrane integrity during late elongation of the embryo. *Mol. Biol. Cell* 22, 3331–3343.

Trier, J.S., Allan, C.H., Abrahamson, D.R., and Hagen, S.J. (1990). Epithelial basement membrane of mouse jejunum. Evidence for laminin turnover along the entire crypt-villus axis. *J. Clin. Invest.* 86, 87–95.

Trzebiatowska, A., Topf, U., Sauder, U., Drabikowski, K., and Chiquet-Ehrismann, R. (2008). *Caenorhabditis elegans* teneurin, ten-1, is required for gonadal and pharyngeal basement membrane integrity and acts redundantly with integrin ina-1 and dystroglycan dgn-1. *Mol. Biol. Cell* 19, 3898–3908.

Tsilibary, E.C. (2003). Microvascular basement membranes in diabetes mellitus. *J. Pathol.* 200, 537–546.

Unsoeld, T., Park, J.O., and Hutter, H. (2013). Discoidin domain receptors guide axons along longitudinal tracts in *C. elegans*. *Dev. Biol.* 374, 142–152.

Urbano, J.M., Torgler, C.N., Molnar, C., Tepass, U., López-Varea, A., Brown, N.H., de Celis, J.F., and Martín-Bermudo, M.D. (2009). *Drosophila* laminins act as key regulators of basement membrane assembly and morphogenesis. *Development* 136, 4165–4176.

van den Berg, M.C.W., MacCarthy-Morrogh, L., Carter, D., Morris, J., Ribeiro Bravo, I., Feng, Y., and Martin, P. (2019). Proteolytic and opportunistic breaching of the basement membrane zone by immune cells during tumor initiation. *Cell Rep.* 27, 2837–2846.e4.

Vogel, B.E., and Hedgecock, E.M. (2001). Hemicentin, a conserved extracellular member of the immunoglobulin superfamily, organizes epithelial and other cell Attachments into oriented line-shaped junctions. *Development* 128, 883–894.

Walser, M., Umbricht, C.A., Fröhli, E., Nanni, P., and Hajnal, A. (2017).  $\beta$ -integrin de-phosphorylation by the Density-Enhanced phosphatase DEP-1 attenuates EGFR signaling in *C. elegans*. *PLoS Genet.* 13, e1006592.

Woo, W.M., Berry, E., Hudson, M.L., Swale, R.E., Goncharov, A., and Chisholm, A.D. (2008). The *C. elegans* F-spondin family protein SPON-1 maintains cell adhesion in neural and non-neural tissues. *Development* 135, 2747–2756.

Xiong, J.P., Stehle, T., Diefenbach, B., Zhang, R., Dunker, R., Scott, D.L., Joachimiak, A., Goodman, S.L., and Arnaut, M.A. (2001). Crystal structure of the extracellular segment of integrin  $\alpha$ V $\beta$ 3. *Science* 294, 339–345.

Yurchenco, P.D. (2011). Basement membranes: cell scaffoldings and signaling platforms. *Cold Spring Harb. Perspect. Biol.* 3, a004911.

Yurchenco, P.D. (2015). Integrating activities of laminins that drive basement membrane assembly and function. *Curr. Top. Membr.* 76, 1–30.

Yurchenco, P.D., and Patton, B.L. (2009). Developmental and pathogenic mechanisms of basement membrane assembly. *Curr. Pharm. Des.* 15, 1277–1294.



## STAR★METHODS

### KEY RESOURCES TABLE

REAGENT or RESOURCE	SOURCE	IDENTIFIER
<b>Bacterial and Virus Strains</b>		
RNAi feeding strain	<i>Caenorhabditis</i> Genetics Center	HT115 (DE3)
Vidal RNAi Library	Open Biosystems	ORF RNAi Collection V1.1
Ahringer RNAi Library	Source Bioscience	<i>C. elegans</i> RNAi Collection (Ahringer)
<b>Chemical, Peptides, and Recombinant Proteins</b>		
MitoTracker Red CMXRos	Molecular Probes	M7512
Dicyclohexylcarbodiimide (DCCD)	Sigma	633267
Ethyl 3-aminobenzoate methanesulfonate (Tricaine)	Sigma	E10521
Levamisole hydrochloride	Sigma	1359302
2,3-Butanedione monoxime (BDM)	Sigma	B0753
MitoTracker Red CMXRos	Molecular Probes	M7512
4x Laemmli Sample Buffer	BIO RAD	1610747
Anti-mNeonGreen antibody	chromotek	32F6
HRP-conjugated secondary antibody	Jackson ImmunoResearch	115-035-003
Supersignal West Pico Chemiluminescent Substrate	ThermoFisher Scientific	34579
<b>Experimental Models: Organisms/Strains</b>		
<i>C. elegans</i> wild-type strain	<i>Caenorhabditis</i> Genetics Center	WB-STRAIN:N2_(ancestral)
emb-9p::emb-9::mCh transgene; qyls46	Ihara et al., 2011	NK364
emb-9p::emb-9::mCh transgene; qyls44	Ihara et al., 2011	NK362
emb-9p::emb-9::mCh transgene with mig-6L mutant; qyls46; mig-6(oz113)/nT1	qyls46 (Ihara et al., 2011)	NK2546
emb-9p::emb-9::mCh transgene with lam-2::mNG CRISPR knock-in; qyls44; qy20	qyls44 (Ihara et al., 2011), qy20 (this study)	NK2545
emb-9p::emb-9::mCh transgene with mig-6S::mNG/+ CRISPR knock-in; qyls46; qy72/+	qyls46 (Ihara et al., 2011), qy72 (this study)	NK2544
emb-9::mNG CRISPR knock-in; qy24	This study	NK2326
emb-9::mEos2 CRISPR knock-in; qy89	This study	NK2604
let-2::LL::mNG CRISPR knock-in; qy61	This study	NK2558
lam-1::LL::mNG (9aa linker) CRISPR knock-in; qy63	This study	NK2123
lam-2::LL::mNG CRISPR knock-in; qy20	This study	NK2335
lam-2::LL::mNG CRISPR knock-in with plasma membrane mCherry; qy20;cpls55	This study	NK2336
lam-2::LL::mNG CRISPR knock-in; qy41	Jayadev et al., 2019	NK2446
lam-3::LL::mNG CRISPR knock-in; qy28	This study	NK2425
epi-1::LL::mNG CRISPR knock-in; qy31	This study	NK2404
mNG::mig-6N terminal CRISPR knock-in; qy37	This study	NK2442
mig-6S::LL::mNG CRISPR knock-in; qy72/+	This study	NK2556
mig-6L::LL::mNG CRISPR knock-in; qy73	This study	NK2557
unc-52::mNG C terminal CRISPR knock-in; qy53	This study	NK2500
mNG::unc-52 N terminal CRISPR knock-in; qy75	This study	NK2555

(Continued on next page)

**Continued**

REAGENT or RESOURCE	SOURCE	IDENTIFIER
unc-52::mNG synthetic exon CRISPR knock-in; qy80	This study	NK2583
nid-1::LL::mNG CRISPR knock-in; qy38	This study	NK2443
cle-1::LL::mNG CRISPR knock-in; qy22	This study	NK2322
mNG::fbl-1 N terminal CRISPR knock-in; qy62	This study	NK2579
agr-1::LL::mNG CRISPR knock-in; qy27	This study	NK2353
spon-1::LL::mNG CRISPR knock-in; qy30	This study	NK2580
pxn-1::LL::mNG CRISPR knock-in; qy40	This study	NK2445
mNG::pxn-2 N terminal CRISPR knock-in; qy76	This study	NK2565
pxn-2::LL::mNG C terminal CRISPR knock-in; qy39	This study	NK2444
ost-1::LL::mNG CRISPR knock-in; qy60	This study	NK2559
him-4::LL::mNG CRISPR knock-in; qy33	This study	NK2422
ina-1::LL::mNG CRISPR knock-in; qy23	<a href="#">Jayadev et al., 2019</a>	NK2324
ina-1::LL::mKate CRISPR knock-in; qy46	This paper	NK2476
pat-2::LL::mNG CRISPR knock-in; qy26	<a href="#">Jayadev et al., 2019</a>	NK2330
pat-2::LL::2XmNG CRISPR knock-in; qy49	<a href="#">Jayadev et al., 2019</a>	NK2479
pat-3::LL::mNG CRISPR knock-in; qy36	<a href="#">Jayadev et al., 2019</a>	NK2436
gpn-1::LL::mNG CRISPR knock-in; qy35	This study	NK2581
lon-2::LL::mNG CRISPR knock-in; qy55	This study	NK2582
dgn-1::LL::mNG CRISPR knock-in; qy18	<a href="#">Naegli et al., 2017</a>	NK2318
ten-1::LL::mNG CRISPR knock-in; qy56	This study	NK2502
ddr-1::LL::mNG CRISPR knock-in; qy43	This study	NK2456
ddr-2::LL::mNG CRISPR knock-in; qy44	This study	NK2457
ptp-3::LL::mNG CRISPR knock-in; qy47	This study	NK2477
sdn-1::LL::mNG CRISPR knock-in; qy29	This study	NK2413
dgn-2::LL::mNG CRISPR knock-in; qy 82	This study	NK2587
gon-1::LL::mNG CRISPR knock-in; qy45	This study	NK2590
mig-17::mNG::3xFlag; shc19	<a href="#">Ji et al., 2019</a>	FDU1506
<b>Recombinant DNA</b>		
pDD122 (Peft-3::Cas9 + ttTi5605 sgRNA)	Addgene	47550
mNG-C1 <sup>Δ</sup> SEC <sup>Δ</sup> linker	This study	mNG-SEC-LL
mNG-C1 <sup>Δ</sup> SEC <sup>Δ</sup> bothlink	This study	mNG-SEC-bothlink
mEos2-C1 <sup>Δ</sup> SEC	This study	mEos2-SEC
L4440 RNAi empty vector control	Addgene	1654
mig-6 RNAi	This study / Ahringer	mig-6 RNAi
<b>Software and Algorithms</b>		
Fiji	<a href="#">Schindelin et al., 2012</a>	Image J 2.0.0-rc-69/1.52p, <a href="http://fiji.sc/">http://fiji.sc/</a>
Photoshop	Adobe	Version CC 2018
Imaris	Bitplane	Version 9
Illustrator	Adobe	Version CC 2018
R	GNU Project	Open Source
μManager	<a href="#">Edelstein et al., 2014</a>	Version 1.4, <a href="https://micromanager.org/">https://micromanager.org/</a>
iLas	Biovision	V.1.2.3
MetaMorph	Molecular Devices	7.10.3.279
Excel	Microsoft	Version 15.39
GraphPad Prism	GraphPad	Version 7

## RESOURCE AVAILABILITY

### Lead Contact

Further information and requests for resources and reagents should be directed to and will be fulfilled by the Lead Contact, David R. Sherwood ([david.sherwood@duke.edu](mailto:david.sherwood@duke.edu)).

### Materials Availability

All worm strains will be available from the Caenorhabditis Genomics Center (CGC, [cgc.umn.edu](http://cgc.umn.edu)).

Plasmids generated in this study are available upon request.

### Data and Code Availability

The published article includes all data generated or analyzed during this study.

## EXPERIMENTAL MODEL AND SUBJECT DETAILS

### Worm Handling and Strains

Worms were grown under standard conditions and N2 Bristol strain was wild type. L1 animals were obtained by bleach synchronization. All worms used in this study were hermaphrodites. L4 animal staging was determined by DIC or fluorescence based on gonad and vulval morphology, with gonads having reflected, but not completing secondary migration. All alleles and strains used in this study are listed in Key Resources and annotated according to wormbase guidelines: <https://wormbase.org/about/userguide/nomenclature#ecgkh5m87dlji1bf923a064-10>.

## METHOD DETAILS

### CRISPR Strain Construction

We used CRISPR/Cas9-mediated genome editing with a self-excising hygromycin selection cassette (SEC) to generate endogenous BM tags with modifications from previous methods ((Dickinson and Goldstein, 2016; Jayadev et al., 2019); Table S1; Figures S1 and S2). Briefly, we generated new SEC plasmids by removing the 3xFlag tag downstream of the SEC cassette sequence and attached an 18 amino acid flexible linker (flexlink) (6x glycine-alanine-serine) in frame and directly upstream of the fluorophore. For most genes the fluorophore was inserted just upstream of the stop codon to generate a C-terminally tagged protein. However, in cases where there were multiple isoforms that shared an N-terminus but varied at the C-terminus, we generated an N-terminal knockin. For N-terminal knock-ins, we ran a signal peptide prediction (SignalP-5.0) to determine signal peptide cleavage sites and inserted the fluorophore immediately downstream of the site. For all N-terminal knock-ins, we used a 2aa upstream linker and 4aa downstream linker strategy (bothlink) (Morin et al., 2001), except for papilin/*mig-6*, for which we used the flexlink cassette with 18aa amino acid linker being present on the N-terminus. The papilinS isoform-specific tag prevented splicing of the papilinL isoform, resulting in homozygous animals that exhibit sterility and gonad phenotypes consistent with loss of papilinL (Kawano et al., 2009). We thus reported values for heterozygous (papilinS::mNG/+) animals in all analyses. In the specific cases of *emb-9* and *let-2*, we used the bothlink cassette to insert the mNG in the same locus as the endogenous *vkg::GFP* in *D. melanogaster* (Morin et al., 2001). To generate the internally tagged perlecan/*unc-52* we inserted a synthetic exon (Morin et al., 2001) between two exons near the C-terminus of the gene (Figures S1 and S2; Table S1). For all constructs 2-3kb of DNA centered on the insertion site was amplified from N2 genomic DNA and cloned into an intermediate vector (TOPO) to be used as homology arms. Homology arms were mutated to introduce as many silent point mutations as possible adjacent to the Cas9 cut site. No mutations were made for *epi-1*, *let-2*, *pxn-2*, *unc-52* C-terminal, or *unc-52* exon as the insertion split the PAM site. For *ost-1* and *ten-1* only one silent mutation could be introduced, for all other constructs 5-13 mutations were introduced between the two sgRNA sites chosen. Mutated homology regions were inserted into the appropriate repair plasmid using Gibson assembly. We generated 1 or 2 guide RNA (sgRNA) plasmids for each target by inserting the respective sgRNA sequences into the pDD122 plasmid. The sgRNA sequences used are listed (Figures S1 and S2; Table S1).

For each strain, we injected a mixture of 50ng/μl Cas9-sgRNA plasmids (25ng/μl of each guide plasmid in cases where two sgRNAs were available), 50-100ng/μl repair template plasmid, and 2.5ng/μl pCFJ90 (*myo-2p>mCherry* as a co-injection marker) into the gonads of ~10-40 young adult N2 animals. Injected animals were singled and allowed to lay eggs for 3-4 days at 20-23°C in the absence of selection. 500μl of 2mg/ml hygromycin solution was added to each plate, and the plates were returned to 20°C for 4-5 days. Candidate knockin animals were dominant roller [*sqt-1(e1350)*] worms that survived hygromycin treatment and lacked red fluorescent extrachromosomal array markers. To excise the SEC, we heat-shocked plates containing ~6 L3/L4 rollers each at 34°C in a water bath for 4 h, then grew the animals at 20°C for 3-4 days. Adult wild-type animals (worms that lost both copies of the SEC) were singled and successful genome editing was verified by visualizing fluorescence and PCR genotyping. Sequencing of the fluorophore insertion site was also performed in all cases to verify proper insertion.

### CRISPR Strain Viability Analysis

We assessed genome-edited strains for viability at the plate level for non-N2 visible phenotypes (e.g., uncoordinated (Unc), lethal (Let), dumpy (Dpy), and sterile (Ste)). To assess viability, edited worms were compared to N2 at 20°C. Five L4 animals were plated

on 200 $\mu$ l of OP50 and allowed to grow until starvation. One day prior to starvation, five L4 animals were picked to new plates for a second generation. This was repeated again for a third generation. If no differences were seen, the worms were considered to have N2 viability.

### Fusion Protein Localization and Cleavage Analysis

To assess the validity of our basement membrane component protein fusions, homozygous viable strains were screened for fluorescence localization using confocal microscopy. Localization of fluorescence in each strain was examined for BM localization and compared to a GFP secreted into the extracellular space. Strains that exhibited a diffuse localization pattern like secreted GFP were analyzed for proteolysis. Amino acid sequences were analyzed using ProP 1.0 (<http://www.cbs.dtu.dk/services/ProP/>) that predicts arginine-lysine cleavage by a proprotein convertase. Proteins that were found to exhibit diffuse fluorescence and possess a cleavage site indicating that the fluorescent protein may be cleaved were removed from analysis and new endogenous tags were generated. Cleavage of the original tag and presence of a full-length protein product from the secondary CRISPR tag were confirmed by Western blot analysis. We did not detect DGN-2::mNG or GPN-1::mNG fluorescence, suggesting they might be present at low levels or in response to environmental conditions not tested.

### Fusion Protein Western Blot Analysis

Worms were collected in sterile water and washed several times before being pelleted and snap-frozen in liquid nitrogen. Worms were thawed in lysis buffer (2% SDS, 10% glycerol, 50  $\mu$ M Tris 6.8), heated for 5 min at 95°C, then vortexed. Samples were mixed with 4x Laemmli sample buffer (Biorad), heated for 5 min at 95°C, then loaded into a Criterion TGX 10% gel (Biorad) that was run at 100V. The contents of the gel were transferred to nitrocellulose membrane (Biorad) at 20V for 30 min. Membranes were blocked in 5% milk diluted in Tris-buffered saline-Tween 20 (TBS-T) for 1 h before incubation with the anti-mNeonGreen at 1:1000 (32F6, Chromotek) diluted in 2.5% milk/TBS-T. After washing, horseradish peroxidase (HRP)-conjugated secondary antibodies (Jackson-ImmunoResearch) were diluted in 5% milk/TBS-T. SuperSignal West Pico Chemiluminescent Substrate (Thermo Scientific) was used for detection.

### RNA Interference

RNAi constructs were obtained from the Vidal and Ahringer libraries and all RNAi experiments were performed using the feeding method (Source Bioscience; (Kamath et al., 2003; Rual et al., 2004)). RNAi bacterial cultures were grown in selective media (1:1000 ampicillin) for 12–14 h at 37°C. 1mM Isopropyl  $\beta$ -D-1-thiogalactopyranoside (IPTG) was added to induce dsRNA expression and cultured for an additional hour. RNAi plates were prepared by spreading a 1:1 mixture of 1M IPTG and 100mg/ml ampicillin (5 $\mu$ l each) on NGM agar plates and left at room temperature overnight following seeding with induced RNAi culture to allow for further induction and drying. For co-depletion experiments, the relevant induced bacterial cultures were mixed at a 1:1 ratio before they were seeded on plates. Most experiments were performed using synchronized L1 worms, which were placed on RNAi plates and allowed to feed for 24–72 h at 20°C. The L4440 empty vector was used as a negative control. For depletion of papilin later in development, synchronized L1 worms were fed L4440 bacteria until the L3, 48 h adult, or 72 h adult stages before they were transferred to papilin RNAi plates for 48 h.

### ATP Depletion and Muscle Paralysis

To compare worms immobilized with polystyrene beads alone (muscle contractions, control), L4 hermaphrodites were bathed in 20  $\mu$ M dicyclohexylcarbodiimide (DCCD) in M9 for 1 h (ATP synthase inhibitor) (Hong and Pedersen, 2008), 0.02% levamisole in M9 for 30 min (muscle hypercontraction), 0.2% tricaine and 0.02% levamisole (muscle contraction and relaxant) in M9 for 30 min, or 75mM 2,3-Butanedione monoxime (BDM, muscle relaxant) in M9 for 1 h (Petzold et al., 2011), then transferred to 5% noble agar pads with polystyrene microbeads. The cover slip was partially sealed with VALAP, flooded with relevant buffer or drug solution to prevent the agar from drying, and then fully sealed with VALAP. FRAP analysis was then carried out as outlined below. Importantly, examination of mNG::fibulin levels after all treatments indicated that fibulin levels were not different from control worms ( $n = 5$  for each,  $p > 0.05$ , Student's  $t$ -test).

### Imaging

Confocal images were acquired on a Zeiss AxioImager microscope equipped with a Yokogawa CSU-10 spinning disc confocal controlled by Micromanager (Edelstein et al., 2010) or Metamorph software using a Zeiss 40x Plan-APOCHROMAT 1.4NA oil immersion objective or 100x Plan-APOCHROMAT 1.4NA oil immersion objective and a Hamamatsu ORCA R<sup>2</sup> CCD camera, Orca-Fusion sCMOS camera, or ImageEM EMCCD camera.

For still images of embryonic stages, embryos were collected from OP50 plates, washed with M9, then placed on 5% agar pads with 0.01M sodium azide. Embryo stages were identified under the microscope and acquired at 40x magnification. Exposure times for confocal imaging varied depending on fluorescence intensity (range: 500ms to 1500ms). Images were displayed either as a single z-slice or as confocal maximum intensity z-projections of confocal slices through the embryo.

For images of larval and adult stages, worms were mounted on 5% agar pads containing 0.01M sodium azide. Images were displayed as single z-slice, maximum intensity, or sum intensity projections.



For fluorescence recovery after photobleaching (FRAP) experiments, photobleaching was performed using an iLas<sup>2</sup> targeted laser system from BioVision equipped with an Omicron Lux 60mW 405nm continuous wave laser and controlled with MetaMorph software. Laser power and duration of photobleach were the same for all images within a group of experiments. For all FRAP experiments, worms were immobilized using undiluted 100nm polystyrene bead solution (CV 5%; Polysciences cat. #64010). Duration of experiments and imaging intervals were determined empirically to limit photobleaching. For FRAP experiments where the entire pharynx was photobleached, a slightly higher laser power for a shorter time was used to limit the duration of laser exposure and movement of animals. In all cases the entire surface of the pharynx or gonad was photobleached. To assess the effects of our FRAP conditions on animal health, animals were rescued after posterior pharynx photobleaching and all developed normally ( $n = 30/30$  animals). Further, we never observed pharyngeal morphological defects ( $n > 100$  animals) after photobleaching. Finally, we stained photobleached BMs with mitoTracker Red, which in addition to mitochondria also enriches in intact BMs (Sherwood et al., 2005). BMs stained normally immediately after photobleaching ( $n = 8/8$  animals).

Photoconversion of  $\alpha 1$ -type IV collagen::mEos2 was achieved with the iLas<sup>2</sup> targeted laser system using the following parameters: 0% 405nm laser power, 40 iterations, thickness 3. Photoconversion was limited to the turn region of the gonad in 48 h post-hatching young adult control and papilin RNAi treated animals immobilized on 5% noble agar pads containing 0.01 M sodium azide. Immediately after optical highlighting, animals were recovered, washed in M9, and allowed to feed for 2 h on OP50, then mounted again to determine remaining fluorescence levels of photoconverted  $\alpha 1$ -type IV collagen::mEos2.

To determine gonad surface area, 3D isosurfaces were constructed as previously described (Jayadev et al., 2019) using Imaris software (Bitplane). At 0 h and 24 h treatment timepoints, isosurfaces of the entire developing gonad were generated, but at the 48 h timepoint only images of a single gonad arm could be obtained (because of its large size), and the surface area of the gonad was determined by doubling the surface area of the individual gonad arm.

Parameters for experiments are described in the figure legends. All image and video processing and analysis were performed in Fiji 2.0 (Schindelin et al., 2012). Figures were constructed using Adobe Illustrator (CC 2017), and graphs were exported from R or Microsoft Excel.

### Generation of Model BM Proteins and Receptors for Schematics

For Video S5 three-dimensional models of the BM proteins were generated using structural models from the Research Collaboratory for Structural Bioinformatics Protein Data Bank (RCSB PDB, <https://www.rcsb.org/>) and previously published studies. For collagen IV (chain: 1cag, head: 1m3d) and laminin (alpha: 2y38 (Hussain et al., 2011), 4yeq (Moran et al., 2015), beta: 4aqs (Carafoli et al., 2012), gamma: 5mc) model assembly was based on (Hohenester and Yurchenco, 2013) and references therein. For nidogen (G1: laminin-like G domain - 1pz7 (Stetefeld et al., 2004), G2: 1h4u (Hopf et al., 2001), G3: 1npe (Takagi et al., 2003), and EGF domains (from 1gl4 (Kvansakul et al., 2001)) and the laminin binding site as in 1klo (Stetefeld et al., 1996), the model assembly was based on (Lössl et al., 2014). For agrin (Follistatin-like: 6maa (McCoy et al., 2019), laminin-like-EGF, laminin G: 1pz7 (Stetefeld et al., 2004), and EGF domains, the model based on (Hrus et al., 2007). For fibulin (anaphylatoxin-like: 4hwj (Bajic et al., 2013) and EGF domains, the model assembly based on (Hesselson and Kimble, 2006) For integrins (active form extrapolated from inactive extracellular model 1jv2 (Xiong et al., 2001)). All pdb domains are represented by their solvent-accessible surface models as obtained from Chimera software. The entire protein models were assembled manually. The exact representation of the entire proteins is therefore somewhat artistic (their isoforms / unbound and bound conformations / precise folding may not be accurate). For other BM proteins and receptors that were not modeled in 3D, protein schematic sizes were based off of the number of amino acids in each protein from Wormbase (<https://wormbase.org/>) and shapes were based on the results of conserved domain search using InterPro (<https://www.ebi.ac.uk/interpro/>) as well as structural information from Uniprot (<https://www.uniprot.org/>) to determine which key domains should be represented. The ratio and dynamics of matrix components shown in the BM schematics (Figures 1 and 7C; Video S5) are based on the matrix ratios found in the L1 pharynx (Figure 3) and the dynamics (revealed by FRAP) of each molecule and its mode of movement (Figures 4, 5, S6, and S7).

## QUANTIFICATION AND STATISTICAL ANALYSIS

### BM Composition Comparisons

To compare the composition of the gonadal and pharynx BMs in L1 animals, we used synchronized L1 animals except for perlecan::mNG, for which L1 animals were picked off NGM plates. We first visually screened each strain to determine if the tagged matrix component was present above background levels in the gonadal and pharynx BMs, excluding those that could not be detected. Stacks were acquired with step sizes of 374nm and fluorescence intensity values were generated by drawing an  $\sim 0.5\mu\text{m}$  wide,  $4.5\mu\text{m}$  long line through a clearly defined section of a single confocal z-slice in the mid-plane of the posterior bulb of the pharynx and central dorsal region of the gonadal BM. At least 9 animals were imaged for each matrix component. Background levels were defined by drawing a square region outside the worm and determining the mean intensity. Multiple average background intensities were pooled, and the same background value was subtracted across all strains for consistency to allow for direct comparison. The  $\alpha 1$ -type chain of collagen (EMB-9) is present in two copies per type IV collagen molecule, and was quantified for compositional comparisons, while the  $\gamma$ -chain of laminin (LAM-2) is one of three different chains in laminin and was quantified for comparisons (Kramer, 2005). For simplicity, we used the levels of  $\alpha 1$ -type chain as type IV collagen. To generate waffle plots, the mean intensities of all matrix proteins present in the pharynx or gonad were sorted and all mean values were normalized by dividing by the lowest mean

value (peroxidase-1) and rounding to the nearest whole number. The rounded, normalized value was represented as number of squares in the waffle plot, with the lowest value represented as a single square. Color-coding was kept consistent between waffle plots of gonadal and pharynx BM composition to allow for direct comparison.

### FRAP Analysis

L4 animals were used for most analyses. Levels of perlecan::mNG in the pharynx were too low to accurately measure for FRAP analysis and SPARC::mNG was not analyzed as this strain was not homozygous viable. Background was subtracted as described above. Fluorescence intensity values were generated by drawing an  $\sim 0.5\mu\text{m}$  wide,  $4.5\mu\text{m}$  long line through a clearly defined section of the mid-plane of a single z-slice of the pharynx or gonadal BM at the prebleach time point and measuring this region at each subsequent time point, manually correcting for animal movement. Fluorescence intensity was normalized by: 1) subtracting any residual post-bleach fluorescence from the fluorescence intensity for each time point, 2) dividing each time point by the fluorescence intensity of the pre-bleach time point, and 3) averaging the normalized values. For normalizing the fluorescence intensities in the control region, step 1 was omitted as no photobleaching occurred. For [Figure 4C](#) the mean normalized recovery value at 15 min was of each protein compared to that of  $\alpha 1$ -type IV collagen/EMB-9 using Dunnett's test ( $n = 5$ ). To confirm that our experiments represented the steady-state fluorescence recovery of each protein and not addition of new protein to the BM on top of the existing photobleached protein, we measured a control region for each set of short and long term FRAP experiments to ensure that fluorescence in the BM did not increase significantly during the duration of the experiment (see [Figure S6A](#) for 15-min recovery controls; long term experiments:  $\gamma$ -laminin::mNG - prebleach control region average fluorescence intensity value  $4598 \text{ rfus} \pm 1331 \text{ rfus}$ ;  $\sim 5.5 \text{ h}$  recovery control region average fluorescence intensity value  $4289 \text{ rfus} \pm 1724 \text{ rfus}$ ,  $p = 0.76$ , Student's  $t$ -test.  $\alpha 1$ -type IV collagen::mNG prebleach control region average fluorescence intensity value  $24298 \text{ rfus} \pm 3761 \text{ rfus}$ ;  $\sim 5.5 \text{ h}$  recovery control region average fluorescence intensity value  $24317 \text{ rfus} \pm 6068 \text{ rfus}$ ,  $p = 0.995$ , Student's  $t$ -test).

### Photoconversion Analysis

Mean fluorescence intensity values of photoconverted  $\alpha 1$ -type IV collagen::mEos2 were generated by drawing an  $\sim 0.5\mu\text{m}$  wide,  $2\mu\text{m}$  long line through the photoconverted BM region. Background signal was determined with a similar line in a region outside the BM (but within the worm) with no visible fluorescence. To obtain percentage reduction in mean photoconverted  $\alpha 1$ -type IV collagen::mEos2 signal, the difference between the background-corrected mean photoconverted signal intensities immediately after photoconversion and 2 h after photoconversion was divided by the background-corrected mean photoconverted signal intensity immediately after photoconversion.

### Protein Movement Imaging

To determine mode of recovery of photobleached matrix components, the width of the pharynx was photobleached to limit fluorescence recovery coming from z-planes above or below the imaging plane. Most proteins were assessed for movement in the posterior bulb of the L4 pharynx, however, spondin::mNG recovery was examined in the isthmus and agrin::mNG was examined at the L1 stage where they were present at higher levels. Further, nidogen::mNG and  $\gamma$ -laminin::mNG movement was examined in the bend of L4 gonad arms. For BM components that showed dynamic recovery, imaging intervals were decreased to 6 or 10 s between frames to allow sensitive analysis of initial fluorescence recovery. For analysis of fluorescence recovery, single z-slice images were first registered using the StackReg function in Fiji, then rotated so that the anterior-posterior axis of the pharynx was horizontal with the anterior pharynx facing to the left. For mNG::fibulin, four  $\sim 4\mu\text{m}$  square boxes were drawn: one in the anterior pharynx far from the bleached region, one in an unbleached region adjacent to the bleached region, one at the bleached edge of the bleached region, one  $5\text{--}10\mu\text{m}$  into the bleached region. For all other images, two  $4\mu\text{m}$  square boxes were drawn, one at the bleached edge of the bleached region and the other  $5\text{--}10\mu\text{m}$  into the bleached region. Background was subtracted as described above, and total fluorescence intensity in each box was measured at each time point, normalized to the pre-bleach intensity value in that region, and plotted as a line graph. The rate of matrix movement was determined by assessing the time fluorescently labeled matrix protein was first detected  $5\mu\text{m}$  into the unbleached region and this time was divided into  $5\mu\text{m}$  to determine rate in  $\mu\text{m}/\text{sec}$ . For all recovery experiments at least five animals were examined for each matrix component. To examine recovery in the anterior pharynx, the procorpus was photobleached in L1 agrin::mNG animals and assessed for recovery. Matrix proteins with that showed minimal fluorescence recovery in 30 min were photobleached and reimaged after 1 h (papilinS/MIG-6S) or were rescued back to a plate, and re-mounted and imaged after  $\sim 5.5 \text{ h}$  ( $\gamma$ -laminin/LAM-2,  $\alpha 1$ -type IV collagen/EMB-9). To determine if papilinS,  $\gamma$ -laminin, and  $\alpha 1$ -type IV collagen move within the BM, background was subtracted as above and two  $4\mu\text{m}$  square boxes were drawn, one at the bleached edge of the bleached region and the other  $5\text{--}10\mu\text{m}$  into the bleached region. The total fluorescence intensity in each box was measured, pooled, and the two measurements compared ( $n = 5\text{--}6$  animals for each component). A higher fluorescent signal within the box nearest the bleach site would indicate movement, however, no significant differences in fluorescence intensity between the two boxes was observed in any of the components ([Figure S7D](#)).

To assess the rate of extracellular exchange of a dynamic matrix component with the BM, mNG::fibulin was bleached in the entire pharynx BM and the BM imaged (as outlined above in FRAP analysis) every 10 s for 15 min to assess recovery from extracellular fluid. mNG::fibulin is present at low levels in the gut BM, which is contiguous with the pharynx BM, and thus minimized the contribution of

mNG::fibulin moving within the gut BM and into the pharynx BM after photobleaching. Secreted GFP was also photobleached with similar conditions and over 60% recovered adjacent to the BM in 1 min ( $n = 5$  animals), indicating rapid recovery of the pool of fluorescent protein within the extracellular fluid.

### Papilin Isoform Intensity Comparison

Images were acquired using a spinning disc confocal as described above. Both papilinS::mNG and papilinL::mNG animals were acquired at the same imaging settings to allow for direct comparison of fluorescence intensities. We compared background subtracted mean fluorescence intensities using boxplots and Student's  $t$ -test. Levels of papilinS::mNG were displayed as fold increase above papilinL::mNG levels by taking the mean fluorescence intensity of the papilinS::mNG animals divided by the papilinL::mNG animals. For each experiment ( $n \geq 10$  animals for each).

### RNAi Knockdown Efficiency

To assess the efficiency of papilin RNAi, papilinL::mNG or papilinS::mNG animals from RNAi and control plates were imaged 48 h post plating. Mean gonadal BM fluorescence intensity was measured as described above. Background was subtracted and mean fluorescence intensities were compared using boxplots and Student's  $t$ -tests. Percent knockdown was calculated as the difference between the background-corrected mean fluorescence intensities of animals on the RNAi plate and L4440 control plate divided by the mean fluorescence intensity of animals on the L4440 control plate for each isoform. For L1 platings, 88% reduction of papilinS and 61% reduction of papilinL was observed ( $n = 10$  animals examined each). For the knockdown of papilin later in development, 61%, 69%, and 63% reduction of papilinS was observed with 24 h L3 stage, 48 h adult, and 72 h adult platings, respectively ( $n = 5$ –15 animals for each).

### Scoring of Papilin Knockdown Phenotype

Animals with an endogenous  $\alpha 1$ -type IV collagen::mNG or  $\alpha 1$ -type IV collagen::mCh transgene (*emb-9p>emb-9::mCherry*) were plated on RNAi and assessed for a fibrous type IV collagen network 48 h after plating. To assess the relationship between patterning of residual papilin and fibrous type IV collagen after papilin depletion, L1 stage papilinS::mNG; the  $\alpha 1$ -type IV collagen::mCh worms were placed on papilin RNAi and imaged after 48 h. Maximum intensity projections of the gonad were generated and an  $\sim 0.5 \mu\text{m}$  wide line was drawn through a region where the type IV collagen network had a fibrous appearance and patches of residual papilinS::mNG were present. Background was subtracted and fluorescence intensities were normalized and plotted on a line graph.

### Quantification of ADAMTS Localization Following Papilin Knockdown

To quantify the localization of GON-1::mNG, MIG-17::mNG, peroxidasin-2::mNG, and peroxidasin-1::mNG following papilin RNAi knockdown, L1 animals were plated on papilin RNAi and were imaged at  $\sim 48$  h post plating. Quantification of BM fluorescence intensity was assessed by generating a three-slice sum projection in each animal and drawing a  $0.5 \mu\text{m}$  wide line along the BM at the turn of the gonad. Background was subtracted and mean fluorescence intensities were compared using boxplots and Student's  $t$ -tests ( $n \geq 10$  animals for each).

### Statistical Analysis

For quantification of fluorescence levels, sample size was validated a posteriori for variance and statistical significance. Statistical analysis was performed in R using the stats package (stats v3.6.1) unless otherwise specified. Distribution of data was assessed for normality using the Shapiro-Wilk test. For comparisons of mean fluorescence intensities between two populations, we used an unpaired, two-tailed Student's  $t$ -test. To compare mean fluorescence recovery of multiple samples to a single control, we performed one-way ANOVA followed by a post-hoc Dunnett's test (DescTools v0.99.19). Waffle plots and FRAP line graphs were prepared in R using the ggplot2 package and boxplots were prepared in GraphPad Prism. In boxplots, box edges depict the 25<sup>th</sup> and 75<sup>th</sup> percentiles, the line in the box indicates the median value, and whiskers mark the minimum and maximum values. All other bar and line graphs were prepared in Microsoft Excel. Figure legends indicate sample sizes, statistical tests used, and  $p$ -values.

**Developmental Cell, Volume 54**

## **Supplemental Information**

### **Comprehensive Endogenous Tagging of Basement Membrane Components Reveals Dynamic Movement within the Matrix Scaffolding**

**Daniel P. Keeley, Eric Hastie, Ranjay Jayadev, Laura C. Kelley, Qiuyi Chi, Sara G. Payne, Jonathan L. Jeger, Brenton D. Hoffman, and David R. Sherwood**



# Keeley et al., Figure S1

## BM COMPONENTS

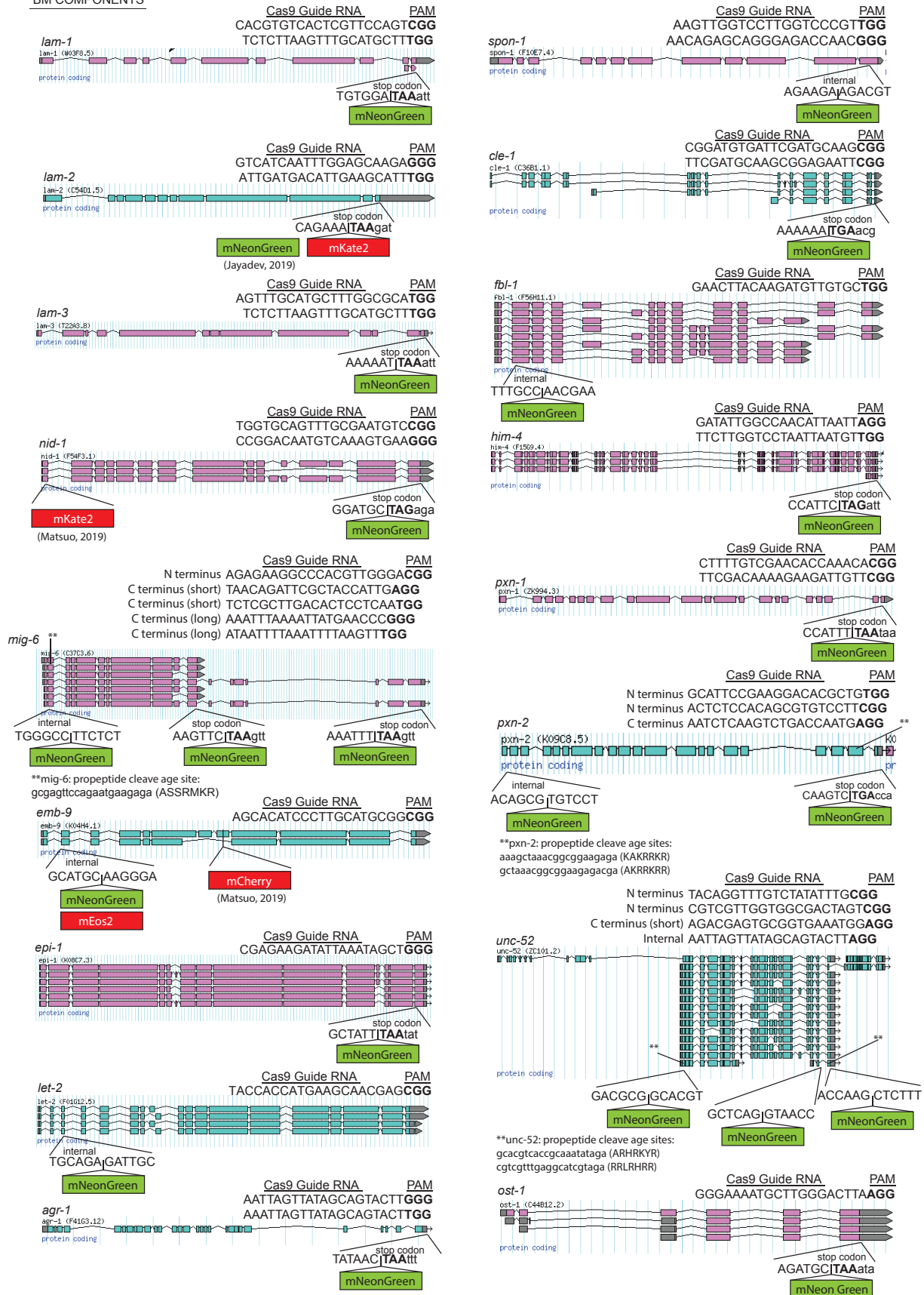
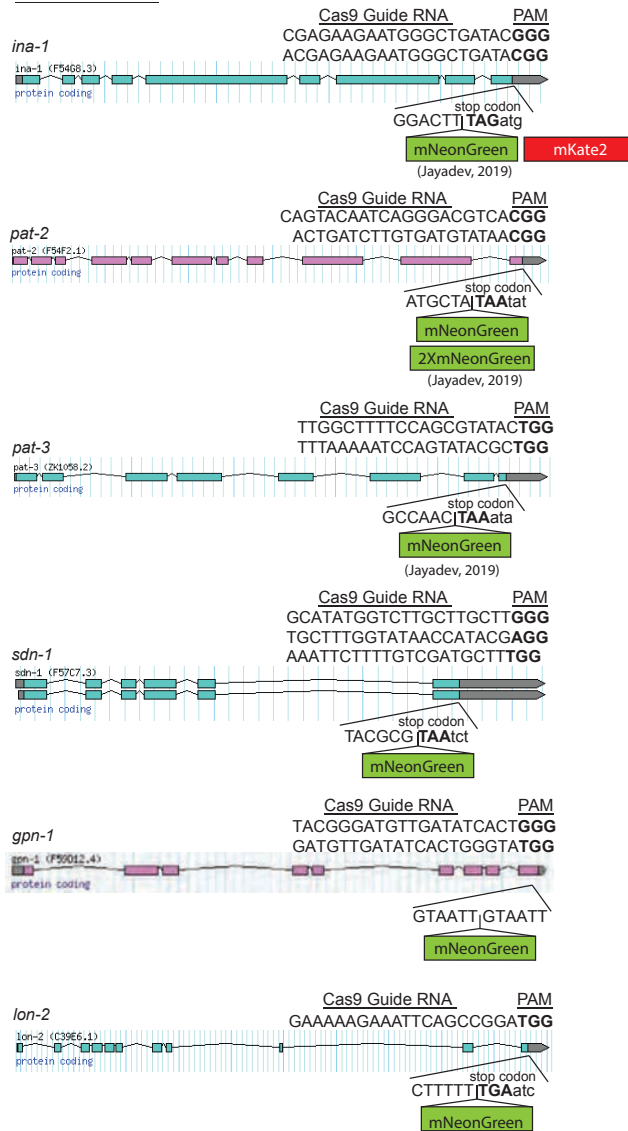


**Figure S1. Fluorophore insertions into BM matrix encoding genes. Related to Figure 1.**

Gene schematics derived from wormbase.org for each BM component CRISPR knock-in strain indicate the genomic location and fluorophore used to create the gene fusion for each strain. For each gene schematic, the sgRNA sequence(s) and PAM site used to target the gene are shown. Below each schematic is the sequence where the fluorophore was inserted into the gene. Each gene was tagged with mNeonGreen (green box), mKate2 (red box), or mEos2 (red box). For genes that were tagged at multiple loci, each knock-in site is shown. Sequences of putative proprotein convertase cleavage sites in papilin (*mig-6*), peroxidasin-2, and perlecan (*unc-52*) are listed and denoted with a double asterisk (\*\*). Knock-in sites for previously published tags are displayed with citations.

# Keeley et al., Figure S2

## BM RECEPTORS



## ADAMTS

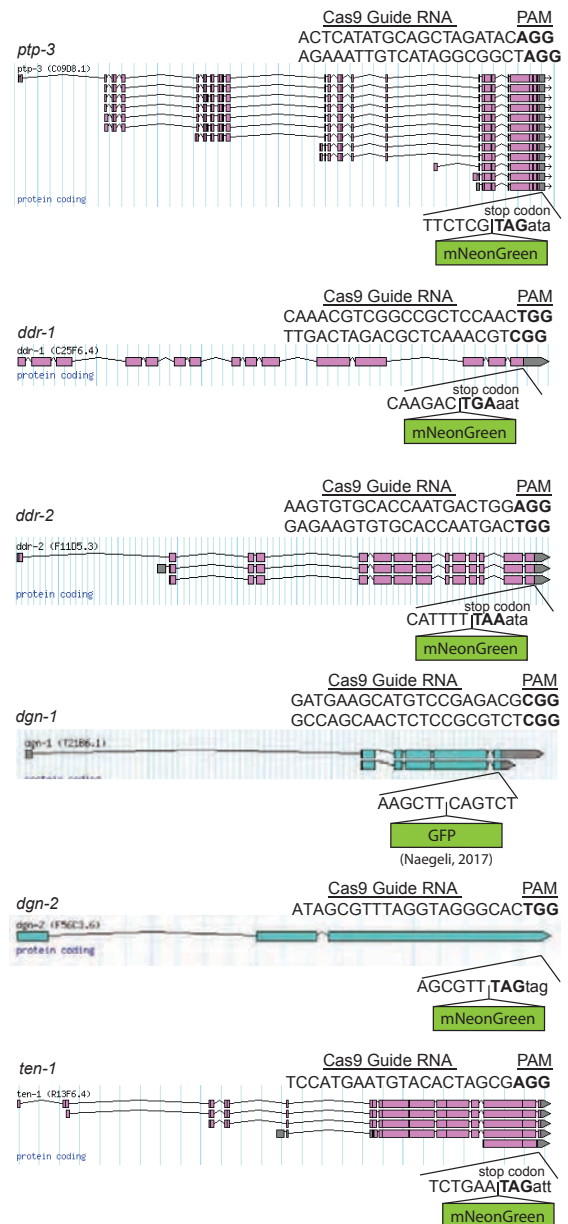


**Figure S2. Fluorophore insertions into receptors and *gon-1*, Related to Figures 1 and 7.**

Gene schematics obtained from wormbase.org encoding each BM receptor CRISPR knock-in strain indicate the genomic location where the fluorophore was inserted. For each gene the sgRNA sequence and PAM site used are shown above the gene. Below each schematic is the sequence where each fluorophore was inserted. Each gene was tagged with mNeonGreen (green box) or mKate2 (red box). For genes that were tagged at multiple loci, each knock-in site is shown. The knock-in sites for previously published tagged genes are displayed with citations.



Keeley et al., Figure S3

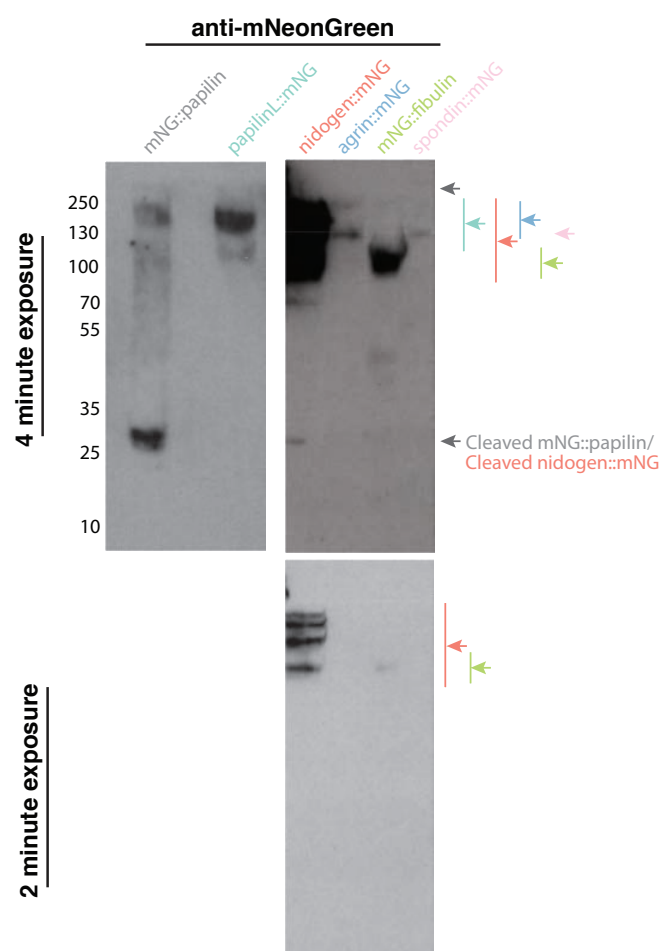


**Figure S3. Western blots of mNG tagged BM proteins. Related to Figure 1.**

Western blots of mNG tagged BM proteins using anti-mNG primary antibody for N-terminally tagged mNG::papilin, C-terminally tagged papilinL::mNG, nidogen::mNG, agrin::mNG, mNG::fibulin, and spondin::mNG. A faint full sized ~150kDa band in the N-terminally tagged mNG::papilin, as well as a much brighter band that ran at the size of mNG (~30 kDa) was detected (n = 3/3 trials). PapilinL::mNG lane shows a predominant ~150 kDa band in the lane (as well as a lower molecular weight band ~120 kDa). Lane 4 (space) was removed from the blot due to loading error. Full-length protein products are in agreement with previously published sizes are present for nidogen::mNG (~150-170 kDa(Kang and Kramer, 2000)), agrin::mNG (~160 kDa (Hrus et al., 2007)), mNG::fibulin (~100 kDa (Kubota et al., 2004)), and spondin::mNG runs near its predicted mNG tagged size of 120 kDa. A small fraction of nidogen::mNG appeared to be cleaved.

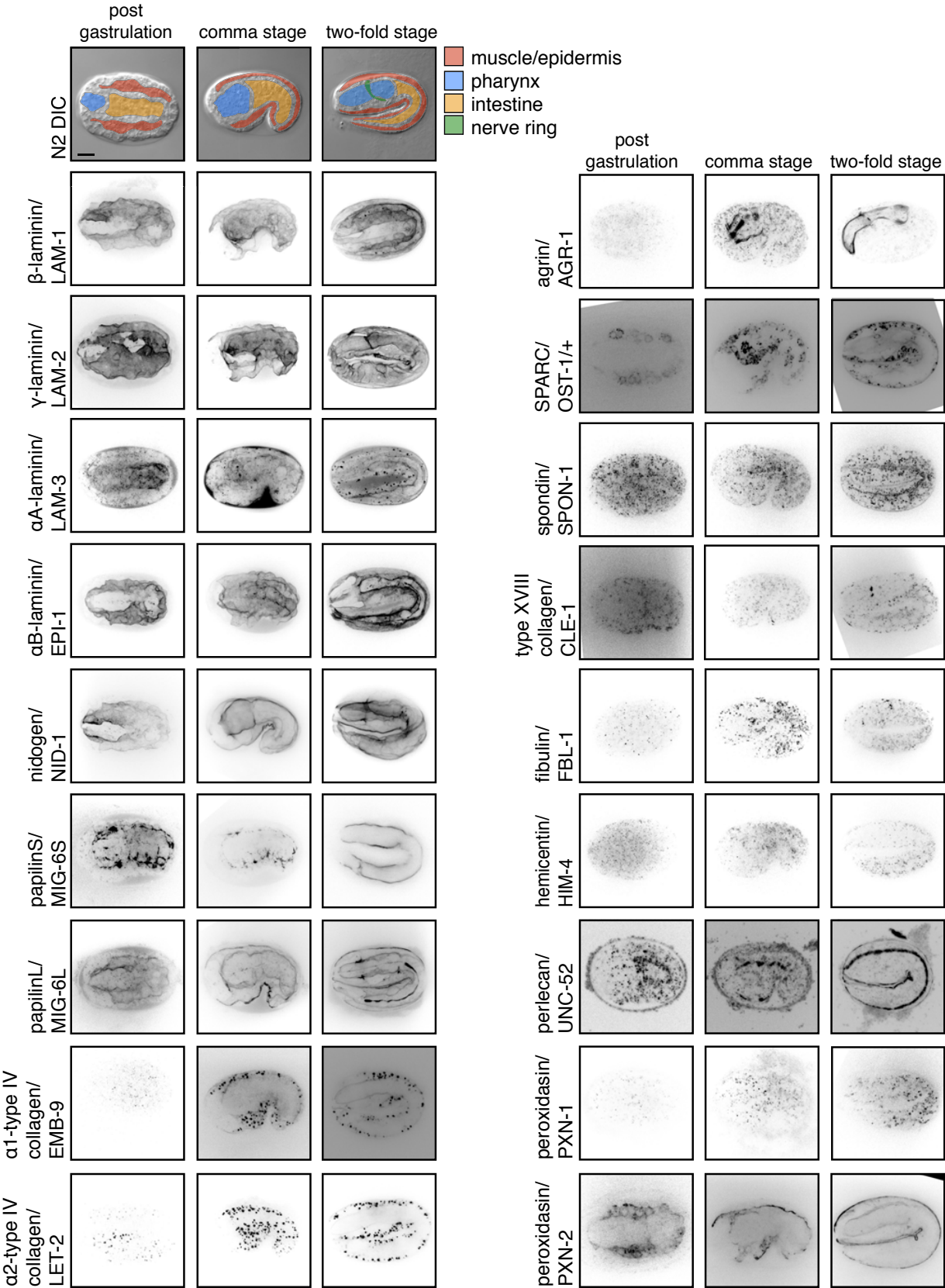


**Figure S4. Localization of BM matrix proteins during embryogenesis. Related to Figure 2.**

Top panel shows DIC images of embryonic development at the post-gastrulation (330 min post-fertilization), comma (430 min), and two-fold stages (490 min). Color overlays highlight embryonic muscle and epidermis (red), primordial pharynx (blue), primordial intestine (yellow) and the nerve ring when it arises at the two-fold stage (green). Inverted grayscale confocal maximum intensity projections of fluorescence localization of representative BM components. For type XVIII collagen/CLE-1 post-gastrulation and two-fold stage and papilinS/MIG-6S two-fold stage, images are displayed as single z-slices. Notably, SPARC was viewed as a heterozygote and  $\alpha 2$ -type IV collagen homozygotes arrest development as L1 larvae. Images are grouped by protein family. ( $n \geq 5$  for every matrix protein at each stage). Scale bar is 10 $\mu$ m.



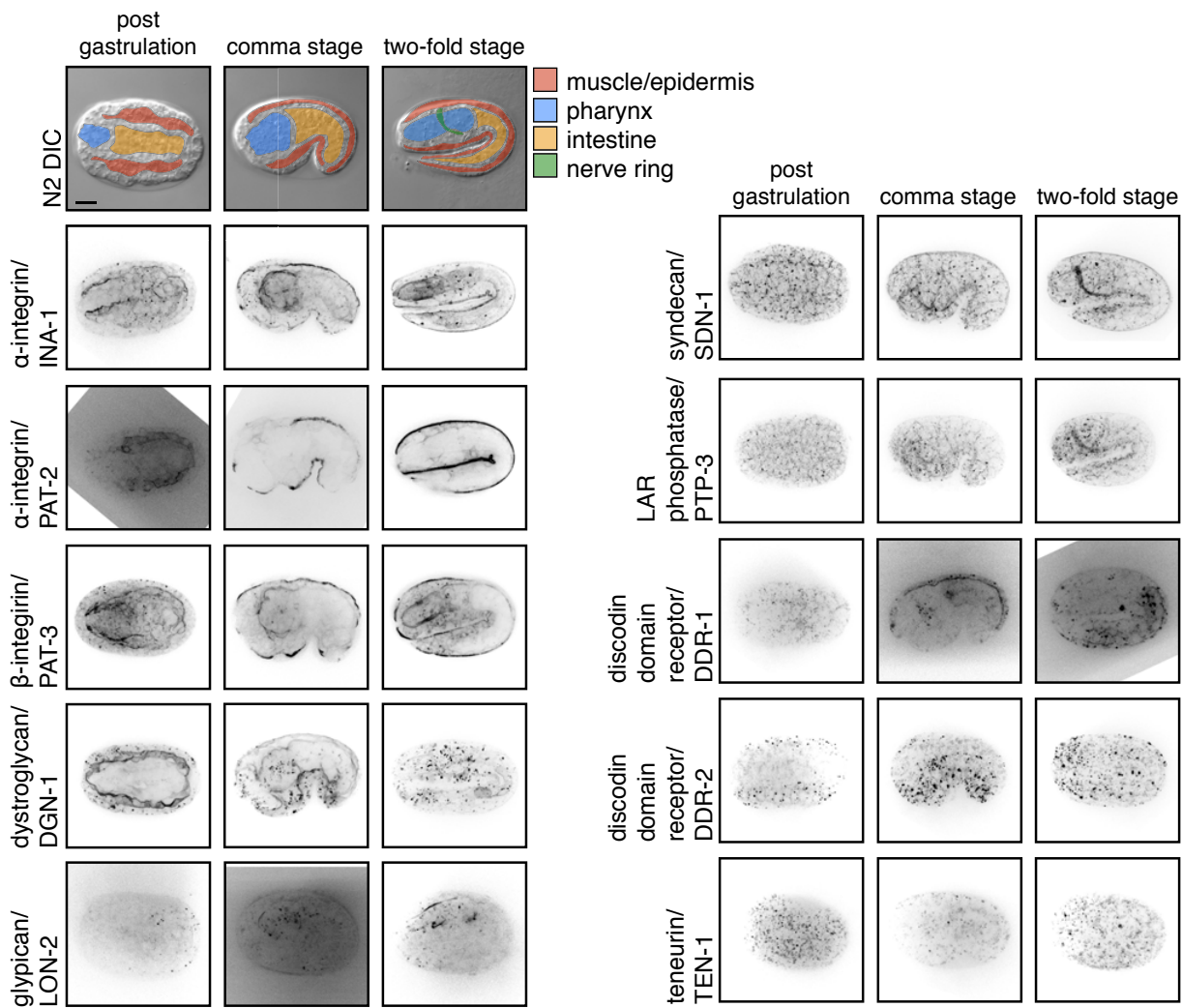
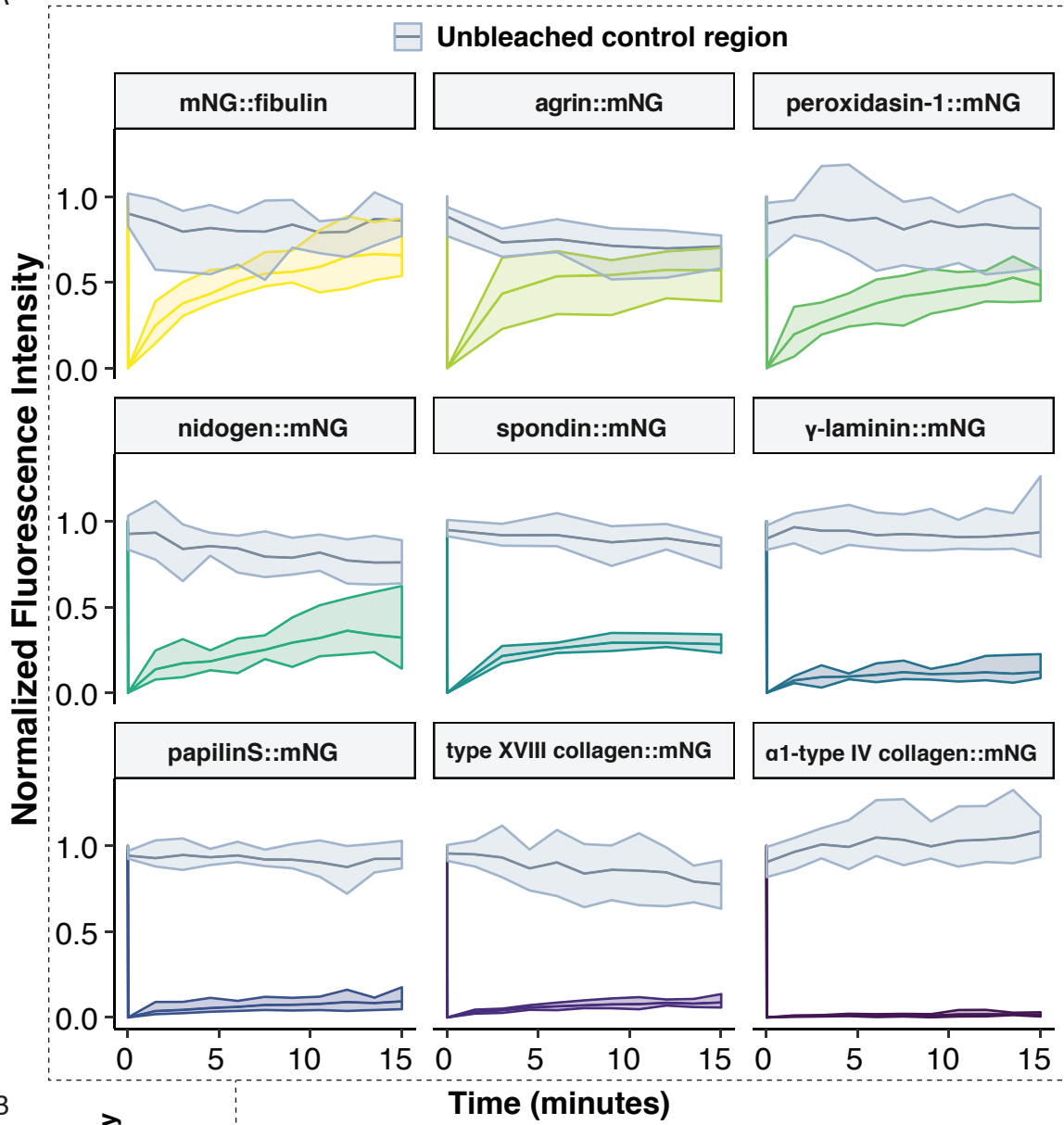


**Figure S5. Localization of BM receptors during embryogenesis. Related to Figure 2.**

Top panel shows DIC images of embryonic development at the post-gastrulation (330 min post fertilization), comma (430 min), and two-fold stages (490 min). Color overlays highlight embryonic muscle and epidermis (red), primordial pharynx (blue), primordial intestine (yellow) and the nerve ring when it arises at the two-fold stage (green). Inverted grayscale confocal maximum intensity projections ( $\alpha$ -integrin/PAT-2 is a single z-slice) of fluorescence localization of representative BM components. Images are grouped by gene family. ( $n \geq 5$  for every matrix receptor at each stage). Scale bar is 10 $\mu$ m.

A



B

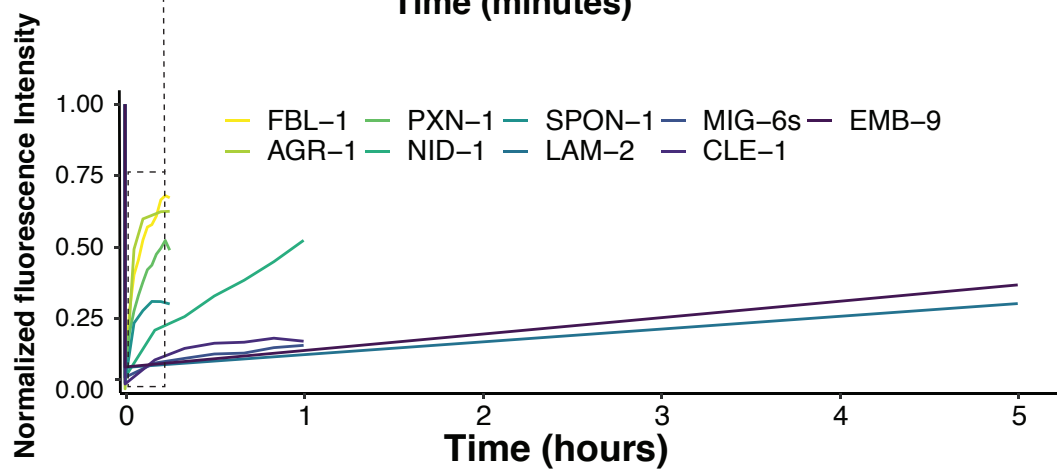


**Figure S6. Long-term FRAP and individual recovery graphs. Related to Figure 4.**

**(A)** Line graphs of FRAP results for each matrix protein shows their average recovery (color for each matrix protein indicated below in B) in the photobleached region compared with the levels in the control region (grey) over a 15-min period at 1.5-min intervals (3-min intervals for agrin::mNG) ( $n = 5$  animals examined for each). Shading indicates the min/max range of the recovery and control regions. **(B)** A line graph shows average fluorescence recovery of each protein on the same plot. Rapidly recovering components displayed over the same 15-min period above. For more stable components, time-lapses were extended until they exhibited 20-30% average recovery. Type XVIII collagen::mNG, and nidogen::mNG were imaged for 1 h at 10-min intervals, while  $\gamma$ -laminin::mNG and  $\alpha 1$ -type IV collagen::mNG were photobleached, recovered to plates, remounted, and imaged 5.5 h later ( $n = 5$  animals for each). Estimated rates of mobility for fast recovering matrix components (fibulin, agrin, peroxidasin-1, nidogen, spondin) are shown in text. The slower recovering type IV collagen, laminin, papilinS, and type XVIII collagen have estimated recovery rates of  $5.6 \pm 1.5\%$ ,  $4.4 \pm 1.0\%$ ,  $11.0 \pm 7.1\%$ , and  $15.0 \pm 5.7\%$  per h, respectively, over the long periods (either 1 h or 5.5 h) they were examined within the pharynx BM ( $n = 5$ , mean  $\pm$  SD).

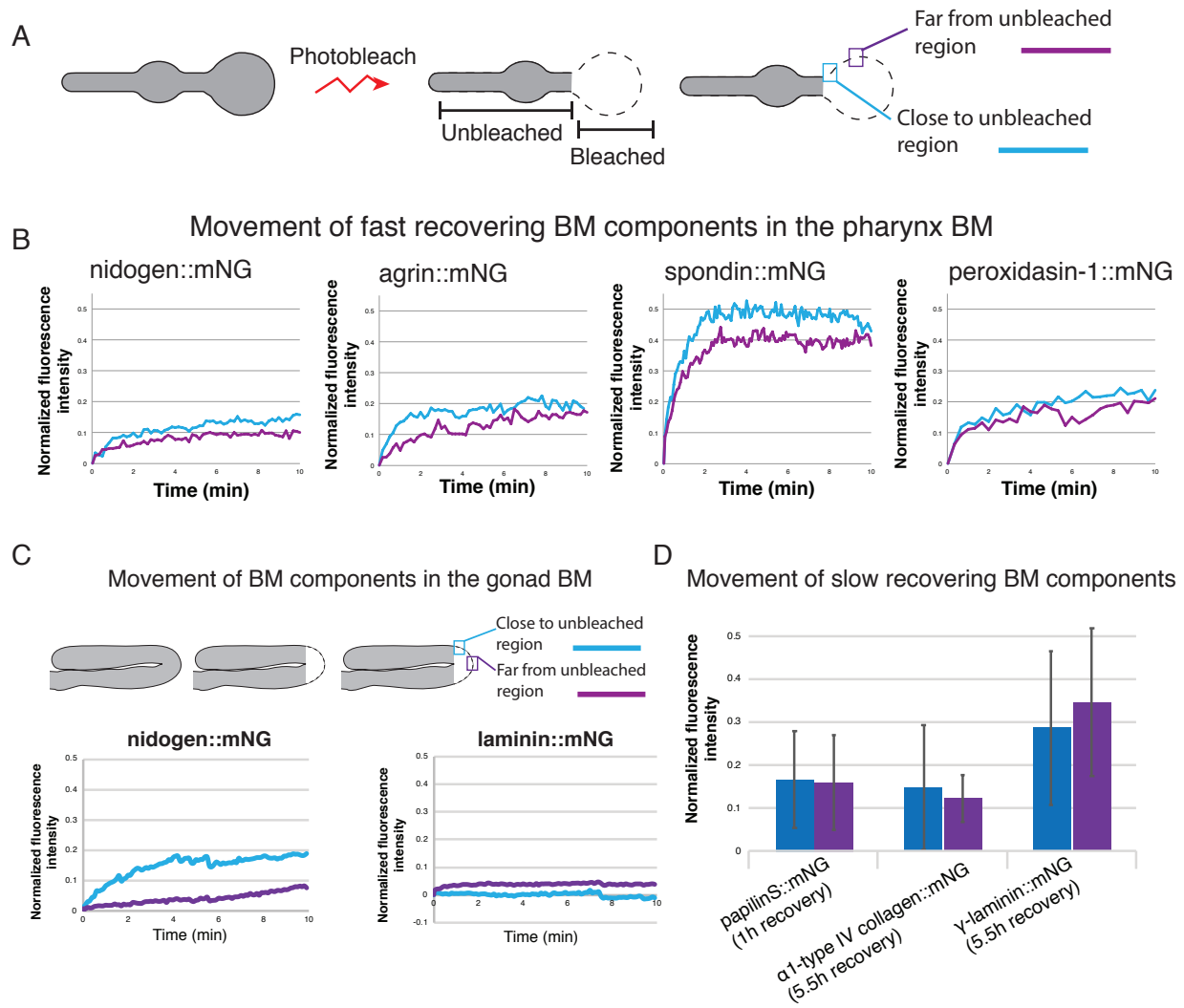




**Figure S7. Dynamic BM proteins move within the BM. Related to Figure 5.**

**(A)** A schematic diagram summarizes the FRAP experiment and analysis to test for movement of dynamic matrix proteins within the BM. The entire posterior bulb (or isthmus for spondin::mNG), was photobleached. Following bleaching, the fluorescence intensity in a region close to the edge of the bleached region (blue box) was compared to intensity in a midregion of the bleached area (purple box) during fluorescence recovery. **(B)** Line graphs of representative experiments for each dynamic matrix protein show faster recovery at the edge of the bleached regions (blue line) versus the middle of the bleached region (purple line,  $n = 5$  for animals for each). **(C)** A schematic diagram summarizes FRAP experiment and analysis to test for movement of matrix components in the gonadal BM in L4 stage animals. The bend in the gonad was photobleached. Following bleaching, the fluorescence intensity in a region close to the edge of the bleached region (blue box) was compared to the intensity in a midregion of the bleached area (purple box) during fluorescence recovery. Line graphs of representative experiments for nidogen and laminin protein show faster recovery at the edge of the bleached regions (blue line) versus the middle of the bleached region (purple line) for nidogen, but not laminin ( $n = 10$  for for each). **(D)** Recovery of more stable components in the pharynx BM was determined as outlined in A, except that analysis was performed on individual images after long periods of recovery. No significant differences in recovery were observed between the region close to the bleached region (blue) and far from the bleached region (purple) for papiinS (1 h recovery),  $\gamma$ -laminin::mNG (5.5 h), and  $\alpha 1$ -type IV collagen::mNG (5.5 h) ( $n = 5-6$  for each,  $p > 0.05$  for each component comparison, Student's  $t$ -test).